Remote Sensing of Environment 240 (2020) 111677

Contents lists available at ScienceDirect

Remote Sensing of Environment

journal homepage: www.elsevier.com/locate/rse

Evaluating impacts of snow, surface water, soil and vegetation on empirical vegetation and snow indices for the Utqiaġvik tundra ecosystem in Alaska with the LVS3 model

Qingyuan Zhang[a,b,*], Tian Yao[a,b], K. Fred Huemmrich[c,b], Elizabeth M. Middleton[b], Alexei Lyapustin[b], Yujie Wang[c,b]

[a] Universities Space Research Association, Columbia, MD 20146, USA
[b] NASA Goddard Space Flight Center, Greenbelt, MD 20771, USA
[c] University of Maryland at Baltimore County, Baltimore, MD 21250, USA

ARTICLE INFO

Edited by Jing M. Chen

Keywords:
Arctic tundra
Vegetation cover fraction (VGCF)
Soil cover fraction (SOILCF)
Snow cover fraction (SNOWCF)
Surface water body cover fraction (WaterBodyCF)
LVS3
MODIS
Hyperion
NDVI
EVI (EVI2)
NIR_v
NDSI

ABSTRACT

Satellite observations for the Arctic and boreal region may contain information of vegetation, soil, snow, snowmelt, and/or other surface water bodies. We investigated the impacts of vegetation, soil, snow and surface water on empirical vegetation/snow indices on a tundra ecosystem area located around Utqiaġvik (formerly Barrow) of Alaska with the Moderate Resolution Imaging Spectrometer (MODIS) images in 2001–2014. Empirical vegetation indices, such as normalized difference vegetation index (NDVI), enhanced vegetation index (EVI), the index of near infrared of vegetation (NIR_v), and modified EVI (EVI2), have been used to monitor vegetation. Normalized difference snow index (NDSI) has been widely applied to monitor snow. The vegetation cover fraction (VGCF), the soil cover fraction (SOILCF), the snow cover fraction (SNOWCF), the surface water body cover fraction (WaterBodyCF), the fractional absorption of photosynthetically active radiation (PAR) by vegetation chlorophyll ($fAPAR_{chl}$), the fractional absorption of PAR by non-chlorophyll components of the vegetation ($fAPAR_{non\text{-}chl}$), and the fractional absorption of PAR by the entire canopy ($fAPAR_{canopy}$) are retrieved with the MODIS images and a coupled Leaf-Vegetation-Soil-Snow-Surface water body radiative transfer model, LVS3. The vegetation indices (NDVI, EVI, EVI2 and NIR_v) differ from VGCF, $fAPAR_{chl}$, $fAPAR_{non\text{-}chl}$, and $fAPAR_{canopy}$. In addition to vegetation, we find that soil, snow and surface water also have impacts on vegetation indices NDVI, EVI (EVI2), and NIR_v. Presence of snow makes lower the observed values of NDVI, EVI2 and NIR_v. After snowmelt is gone, the vegetation indices (NDVI, EVI, EVI2 and NIR_v) linearly decrease with SOILCF and WaterBodyCF, and WaterBodyCF has stronger impacts on these vegetation indices than SOILCF. The relationship between EVI and snow is complicated. NDSI non-linearly increases with SNOWCF, but linearly increases with sum of SNOWCF and WaterBodyCF (sum = 0.5893 × NDSI +0.4342, R^2 = 0.976). NDSI linearly decreases with VGCF, and the relationship between NDSI and SOILCF is complex. Retrievals of VGCF, $fAPAR_{chl}$, $fAPAR_{non\text{-}chl}$ and $fAPAR_{canopy}$ with the LVS3 model provide alternatives for vegetation monitoring and ecological modeling.

1. Introduction

Many attempts to use satellite remote sensing to monitor ecosystem vegetation or snow or surface water have utilized two or three-band empirical indices or other empirical approaches. For instance, previous studies have documented empirical relationships of the two-band normalized difference vegetation index (NDVI) (Tucker, 1979) with the fractional absorption of photosynthetically active radiation (PAR) by a canopy ($fAPAR_{canopy}$) (Huemmrich et al., 2010; Huemmrich and Goward, 1997; Myneni et al., 1997) and with aboveground biomass (Jia et al., 2003; Safari et al., 2018). The NDVI has also been widely used as a proxy for vegetation productivity (Epstein et al., 2015; Gamon et al., 2013; Goetz et al., 2005; Hinzman et al., 2005; Lara et al., 2015, 2018; Myneni et al., 1997; Zhou et al., 2001) and been applied for land cover classification (e.g., Zhang et al., 2018a). In addition to the NDVI, other empirical spectral vegetation indices have been utilized to monitor vegetation from the Moderate Resolution Imaging Spectrometer (MODIS) observations, including the three-band enhanced vegetation index (EVI) (Huete et al.,

* Corresponding author at: NASA/Goddard Space Flight Center, Building 33, Biospheric Sciences Laboratory, Code 618, Greenbelt, MD 20771, USA.
E-mail address: qyz72@yahoo.com (Q. Zhang).

https://doi.org/10.1016/j.rse.2020.111677
Received 7 July 2019; Received in revised form 10 January 2020; Accepted 21 January 2020
Available online 04 February 2020
0034-4257/

2002; Lasseur et al., 2018; Luus et al., 2017; Sims et al., 2008; Walther et al., 2016; Xiao et al., 2004a; Zhang et al., 2015) and the two-band index of near-infrared (NIR) reflectance of vegetation (NIR_v, product of NIR reflectance and NDVI) (Badgley et al., 2017). In order to reduce snow impact on EVI, Jiang and others has developed two-band EVI2 (Jiang et al., 2008). Hydrological models increasingly require snow cover fraction (SNOWCF) in order to provide accurate estimates of snow-covered area within a pixel. The two-band normalized difference snow index (NDSI) determined from MODIS observations along with threshold tests has been used to provide binary maps of snow cover and to provide SNOWCF (Hall et al., 2002; Lv and Pomeroy, 2019; Salomonson and Appel, 2004). A spectral unmixing method was developed to achieve snow cover for pixels mixed with snow and forest (Klein et al., 1998). MODIS observations have also been empirically used to provide binary surface water maps (Carroll et al., 2016; Zhan et al., 2002).

The polar climate of the Barrow peninsula in Alaska is undergoing dramatic changes in temperature, precipitation patterns and soil drainage (ACIA, 2004) and has impacts on these remote sensing empirical indices and approaches over this peninsula. Note that the name of the Barrow peninsula keeps unchanged, but the name of the Barrow town has been changed from Barrow to Utqiaġvik. Tundra occupies a large portion of the peninsula, and lakes, ponds and wetlands cover a significant part of the land surface (Brown et al., 1980; Jia et al., 2003; Lara et al., 2015, 2018). The extent and dynamics of these surface water bodies vary seasonally and inter-annually (Carroll and Loboda, 2017; Hobbie, 1984; Jepsen et al., 2013; Nitze et al., 2017). Snow is common in this region, and is an important part of the regional water cycle and provides an essential feedback to the Earth's heat balance. Snow and snowmelt have impact on water flow across and through soil. For a satellite observation in this region, reflectance may contain contributions from vegetation, soil, surface water and snow (Gamon et al., 2013; Huemmrich et al., 2013; Lara et al., 2018). Soil, snow and surface water can be confounding factors that affect interpretation of the empirical vegetation indices, such as NDVI, EVI, EVI2 and NIR_v (Chang et al., 2019; Goswami et al., 2011; Hope and Stow, 1995; Huete et al., 2002; Luus et al., 2017; Lv and Pomeroy, 2019; Moulin et al., 1997; Myers-Smith et al., 2019; Stow et al., 2004). Vegetation, soil and surface water can also be confounding factors of the empirical snow index NDSI (Chang et al., 2019; Hall et al., 1995, 2002; Lv and Pomeroy, 2019; Zhang et al., 2003).

The fractional absorption of PAR by canopy chlorophyll ($fAPAR_{chl}$) is a descriptor of vegetation photosynthetic potential. The $fAPAR_{non\text{-}chl}$ describes fractional absorption of PAR by non-chlorophyll components of the canopy. We have developed the coupled Leaf-Vegetation-Soil-Snow-Surface water body (LVS3) radiative transfer model to describe pixels mixed with vegetation, snow, soil and/or surface water. Details of the LVS3 model will be provided in Section 2.4. We retrieved cover fractions of vegetation (VGCF), soil (SOILCF), snow (SNOWCF), and surface water body (WaterBodyCF), and $fAPAR_{chl}$, $fAPAR_{non\text{-}chl}$ and $fAPAR_{canopy}$ over the Utqiaġvik (formerly Barrow) tundra ecosystem in Alaska with the LVS3 model, and computed the empirical indices with the same satellite remote sensing observations. The objectives of this study are 1] to demonstrate feasibility of the physical model LVS3 with a 30 m image; 2] to evaluate the impacts of soil, snow and surface water body on NDVI, EVI, EVI2 and NIR_v at the Utqiaġvik tundra ecosystem with MODIS images in 2001–2014; 3] to evaluate the impacts of soil, surface water body and vegetation on NDSI with the MODIS images; 4] to compare the empirical vegetation indices (NDVI, EVI, EVI2 and NIR_v) with bio-variables (VGCF, $fAPAR_{chl}$, $fAPAR_{non\text{-}chl}$, $fAPAR_{canopy}$); and 5] to compare NDSI with SNOWCF.

2. Methods

2.1. Study area

The US-Brw tower site is on tundra of the Alaskan North Slope (http://www.fluxdata.org:8080/sitepages/siteInfo.aspx?US-Brw; location: 71.322526° N, 156.609179° W). The Earth System Research Laboratory (ESRL) Global Monitoring Division (GMD) baseline observatory of the National Oceanic and Atmospheric Administration (NOAA) in Utqiaġvik (formerly Barrow) measures wind, precipitation, air temperature (ftp://aftp.cmdl.noaa.gov/data/meteorology/in-situ/brw/), downwelling and upwelling irradiance (ftp://aftp.cmdl.noaa.gov/data/radiation/baseline/brw/). Rain mainly occurs between July and September. Mean annual wind speed was 4.8 m s^{-1} and mean annual air temperature was −10.4 °C during 2001–2014, with lowest temperature in February (−24.6 °C) and highest temperature in August (+4.2 °C). We used the NOAA ESRL measurements of downwelling and upwelling irradiance to compute broadband albedo, and to determine the snowmelt day: the day of year (DOY) when the albedo dropped below 0.3 (Stone et al., 2002). The natural resources conservation service (NRCS) of the United States Department of Agriculture (USDA) established a soil climate station in 1995. Field soil moisture data, expressed as a unitless volumetric fraction of water (vfw) with units of m^3 water per m^3 soil, were downloaded from https://www.nrcs.usda.gov/wps/portal/nrcs/detail/soils/survey/climate/?cid=nrcs142p2_053676. We selected a 50 × 50 km^2 region centered near the US-Brw site. This study focused on the land area of the region (Fig. 1B). The tundra community in this region is generally classified as moist acidic coastal tundra. Common vascular plants include dwarf shrubs, forbs, and perennial herbs but the most dominant growth forms are graminoids (Brown et al., 1980). In this region common species in wetter areas include *Carex aquatilis, Dupontia fischerii, and Eriophorum spp.*; while drier areas are dominated by *Cassiope tetragona*, *Salix rotundifolia*, and *Luzula confuse (*Hollister et al., 2015*)*. Mosses are a significant portion of the community and may sometimes account for more biomass than vascular plants (Webber et al., 1980). Drained thermokarst lakes are scattered around the study area where physiographic and historical features near the US-Brw site include the North Salt Lagoon, the Imikpuk Lake, the Middle Salt Lagoon, and the South Salt Lagoon (Fig. 1C) (Huemmrich et al., 2013).

2.2. Satellite spectral surface reflectance

We used both MODIS and Hyperion images in this study. The MODIS data over the 50 × 50 km^2 region (Fig. 1B) were processed to 8-day composites in 2001–2014. We chose a point near the US-Brw site as the center of a MODIS 500 m grid (Cheng et al., 2014; Zhang et al., 2014a, 2014b, 2015), and implemented the multi-angle implementation of atmospheric correction (MAIAC) algorithm to process MODIS data (Lyapustin et al., 2011a, 2011b, 2012, 2018). MODIS L1B calibrated radiance data and geolocation data were downloaded from https://ladsweb.nascom.nasa.gov:9400/data/. MODIS L1B radiance data from each swath were gridded at 500 m resolution for bands 1–7: blue (band 3, 459–479 nm), green (band 4, 545–565 nm), red (band 1, 620–670 nm), near infrared (band 2, NIR_1: 841–875 nm; band 5, NIR_2: 1230–1250 nm), and the shortwave infrared (band 6, $SWIR_1$: 1628–1652 nm; band 7, $SWIR_2$: 2105–2155 nm). MAIAC is an advanced algorithm that uses time series analysis and a combination of pixel-based and image-based processing to improve accuracy of cloud/snow detection, aerosol retrievals, and atmospheric correction by incorporating the bidirectional reflectance distribution function (BRDF) model of surface. Recent evaluation (Cooper et al., 2018) showed high quality of MAIAC snow detection. Low quality observations indicated by the QA flag are excluded from further processing.

In addition to MODIS images, we also used one EO-1/Hyperion image in this study. The EO-1/Hyperion was a civilian space-borne spectrometer for Earth observations to collect visible to shortwave infrared (VSWIR) spectral data over a wide variety of study sites in response to user/system requests (Zhang et al., 2012, 2013, 2016). The Hyperion VSWIR spectrometer covered the spectral range of the MODIS bands 1–7. The Hyperion images have a spatial resolution of 30 m. One cloud free and near nadir Hyperion image that covered the US-Brw site

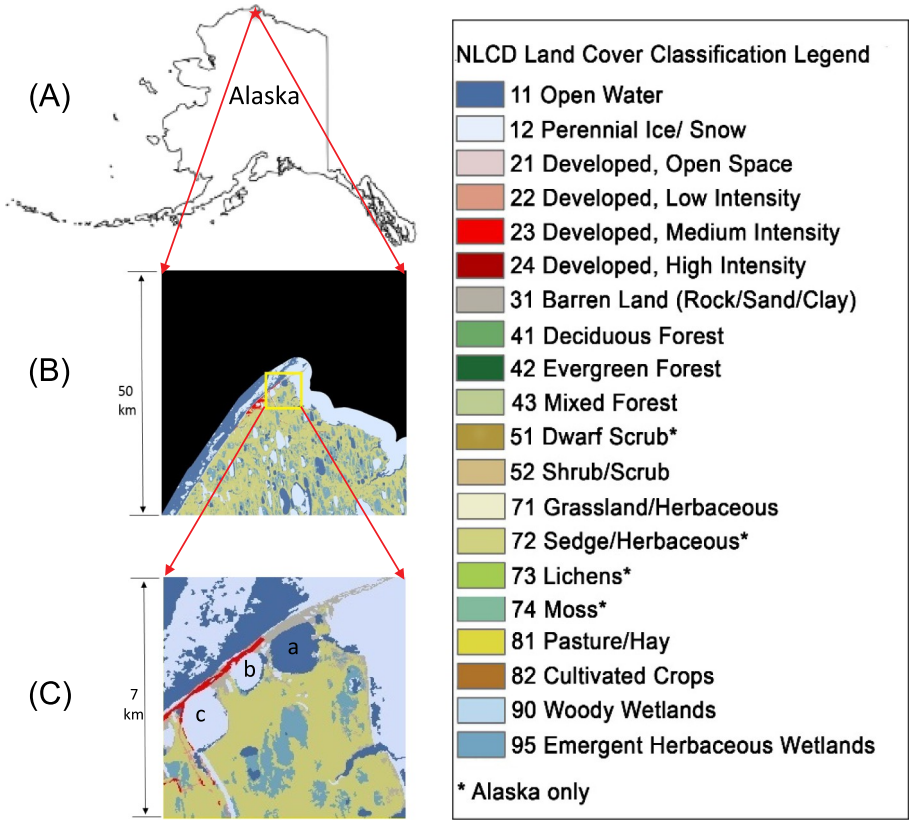

Fig. 1. (A) The location of the US-Brw tundra site (71.32°N, 156.61°W) in Utqiaġvik (formerly Barrow), Alaska;(B) the 50 × 50 km^2 National Land Cover Database (NLCD) 2001 classification map surrounding the US-Brw site; and (C) the 7 × 7 km^2 NLCD (2001) classification map surrounding the US-Brw site, where a is the North Salt Lagoon, b is the Imikpuk Lake, and c is the Middle Salt Lagoon.

was acquired on June 20, 2013. Spatial moment matching was used to de-stripe this Hyperion Level One radiometrically corrected radiance (L1R) image (Sun et al., 2008), and the L1R image was atmospherically corrected using the Atmosphere Removal Algorithm (ATREM) (Gao and Davis, 1997; Gao et al., 1993). In ATREM, the scattering effects due to atmospheric molecules and aerosols were determined with the 6S computer code (Vermote et al., 1997). We subset the atmospherically corrected 30 m Hyperion surface reflectance images for the surrounding 7 × 7 km^2 area of the US-Brw site (Fig. 1C) and derived the broader spectrally MODIS-like bands by convolving the Hyperion bands with the spectral response function (Barry et al., 2002) for the MODIS bands.

We used this 30 m surface reflectance data covering the 7 × 7 km^2 area (Fig. 1C) for visual analysis and evaluation (for objective 1), and used the 8-day 500 m surface reflectance data covering the 50 × 50 km^2 region (Fig. 1B) from 2001 through 2014 to monitor the tundra ecosystem (for objectives 2–5).

2.3. Satellite remote sensing products of vegetation, snow, surface water and soil

In this study, satellite products of vegetation, snow, surface water and soil include their cover fractions, $fAPAR_{canopy}$, $fAPAR_{chl}$ and $fAPAR_{non\text{-}chl}$, and some empirical indices.

Vegetation empirical products from MODIS (500 m) and spectrally MODIS-like (30 m) images include NDVI (Tucker, 1979), EVI, EVI2 (Huete et al., 2002; Jiang et al., 2008), and NIR_v (Badgley et al., 2017):

$$NDVI = \frac{\rho_{NIR_1} - \rho_{red}}{\rho_{NIR_1} + \rho_{red}} \tag{1}$$

$$EVI = 2.5 \times \frac{\rho_{NIR_1} - \rho_{red}}{\rho_{NIR_1} + 6 \times \rho_{red} - 7.5 \times \rho_{blue} + 1} \tag{2}$$

$$EVI2 = 2.5 \times \frac{\rho_{NIR_1} - \rho_{red}}{\rho_{NIR_1} + 2.4 \times \rho_{red} + 1} \tag{3}$$

$$NIR_v = \rho_{NIR_1} \times NDVI \tag{4}$$

Satellite snow empirical product NDSI (Hall et al., 2002) can also be computed with spectral surface reflectance data from Section 2.2:

$$NDSI = \frac{\rho_{green} - \rho_{SWIR_1}}{\rho_{green} + \rho_{SWIR_1}} \tag{5}$$

Cover fractions (VGCF, SOILCF, SNOWCF and WaterBodyCF), $fAPAR_{canopy}$, $fAPAR_{chl}$ and $fAPAR_{non\text{-}chl}$ were retrieved with the LVS3 model described below.

2.4. The coupled radiative transfer model LVS3 and the inversion approach

The coupled radiative transfer model (RTM) LVS3 is coupled with the Leaf RTM PROSPECT, the Vegetation RTM SAIL (Scattering by Arbitrary Inclined Leaves), a Soil model, a Snow model and a Surface water body model. A vegetation canopy can be partitioned into foliage and non-foliage (hereafter referred to as stem) components. Foliage can be further partitioned into chlorophyll, non-photosynthetic pigments (hereafter referred to as brown pigment) and dry matter. Therefore, we can calculate $fAPAR_{canopy}$ (Goward and Huemmrich, 1992), $fAPAR_{chl}$ and $fAPAR_{non\text{-}chl}$ with the following Eqs. (6)–(9):

$$APAR_{canopy} = APAR_{chl} + APAR_{dry\ matter} + APAR_{brown\ pigment} + APAR_{stem} \tag{6}$$

$$fAPAR_{canopy} = \frac{APAR_{canopy}}{PAR_0} \tag{7}$$

$$fAPAR_{chl} = \frac{APAR_{chl}}{PAR_0} \tag{8}$$

$$fAPAR_{non-chl} = \frac{APAR_{dry\ matter} + APAR_{brown\ pigment} + APAR_{stem}}{PAR_0} \tag{9}$$

where PAR_0 is the total incoming PAR, and $APAR_{canopy}$, $APAR_{chl}$, $APAR_{dry\ matter}$, $APAR_{brown\ pigment}$, and $APAR_{stem}$ are absorptions of PAR by the entire canopy, canopy's chlorophyll, dry matter in foliage, brown pigment in foliage, and stem of the canopy, respectively.

PROSPECT is a leaf-level radiative transfer model (Baret and Fourty, 1997; Hosgood et al., 1995; Jacquemoud and Baret, 1990). We use an improved version of PROSPECT in LVS3 to simulate leaf optical properties at MODIS spectral bands 1–7 with five variables: leaf internal structure variable (N); leaf total chlorophyll content (C_{ab}); leaf dry matter content (C_m); leaf water thickness (C_w) and leaf brown pigment (C_{brown}) (Zhang et al., 2005). The SAIL model has been widely used alone or coupled with PROSPECT to simulate vegetation optical properties (e.g., Andrieu et al., 1997; Badhwar et al., 1985; Di Bella et al., 2004; Goel and Deering, 1985; Jacquemoud, 1993; Jacquemoud et al., 2009; Major et al., 1992; Newnham and Burt, 2001; Verhoef, 1984, 1985). The vegetation bio-variables include plant area index (PAI), stem fraction (STEMFR), vegetation cover fraction (VGCF). We successfully developed a two-variable model to mimic soil: soil cover fraction (SOILCF), and soil profile variable ($SOIL_A$) (Zhang et al., 2009, 2012, 2013, 2014a, 2015, 2016). The LVS3 model uses the same soil model. We extend this two-variable method for snow and surface water body in LVS3, adding two snow variables (snow cover fraction, SNOWCF; and snow profile variable, $SNOW_A$) to imitate snow, and adding two water body variables (water body cover fraction, WaterBodyCF; and water body profile variable, $WaterBody_A$) to emulate surface water bodies. The LVS3 model has six groups of variables: (1) observation viewing geometry variables; (2) an atmospheric condition (visibility) variable; (3) bio-variables; (4) soil variables; (5) snow variables; and (6) water body variables (Table 1). The atmospheric visibility variable (VIS, in Table 1) is set to be large and constant throughout this analysis.

Each surface reflectance observation [ρ_{obs}] of MODIS bands (or spectrally MODIS-like bands) 1–7, and associated view zenith angle [θ_v, in degrees], relative view azimuth angle [ϕ, in degrees], and solar zenith angle [θ_s, in degrees] contain some noise, although small differences in angles may be ignored. We treat each reflectance observation as a sample of the following distribution:

$$\rho \sim \{\rho_{obs}(\lambda, \vartheta_v(1 + 3N(0,1)), \vartheta_s(1 + 3N(0,1)), \phi(1 + 3N(0,1)))\} \bullet (1 + 0.05N(0,1)) \tag{10}$$

where N(0,1) is the normal distribution with a mean of zero and SD = 1. We may use as many samples from the distribution (Eq. (10)) as we desire.

We employ the Metropolis algorithm (Braswell et al., 2005; Metropolis et al., 1953; Zhang et al., 2005, 2006), a type of Markov Chain Monte Carlo (MCMC) estimation procedure, to invert the LVS3 model. This method estimates posterior probability distributions of the variables by inspection of the retrieved distributions. At each step, out of a predetermined number of iterations, the algorithm uses the current variable estimate to randomly generate a new "proposal" estimate in variable space. This new variable estimate will be the input for a new model run. Model-retrieved and observed reflectance values are used to calculate the likelihood of an error probability model. The Metropolis algorithm then accepts the new variable estimate with a certain probability. The resulting Markov Chain of accepted variable values converges to the posterior distribution of the variables conditional on the observations after a transient "burn-in" period. MCMC theory assures that such a sampling scheme provides Markov chains whose values represent draws from the posterior distributions. In the following formalism, Pr(·) denotes probability in a general sense, or more specifically, the value of a probability density function. Pr(v) denotes the prior distribution assumed for the set of variables. $Pr(v_{new}|data)$ and $Pr(v_{old}|data)$ refer to the conditional probabilities of "new" and "old" variable estimates (variable points) given the known "data".

We assume a set of independent uniform prior distributions for the variables. Let $X_i = [x_{i1}, \ldots, x_{ip}]$ ($p = 7$), i is the subscript of data point, subscripts 1, …, p mean spectral bands, and x is reflectance. This study assumes that the observed spectral values X_i differ from the model predicted values $U_i = [u_{i1}, \ldots, u_{ip}]$ according to a mean zero p-variate Gaussian error model that results in the likelihood function:

$$L = \prod_{i=1}^{n} \frac{1}{(\sqrt{2\pi})^p |\Sigma|^{1/2}} e^{-(X_i - U_i)'\Sigma^{-1}(X_i - U_i)/2} \tag{11}$$

Table 1
List of variables in the LVS3 model and their search ranges.

	Variable	Description	Unit	Search range
Biophysical variables	PAI	Plant area index, i.e., leaf +stem area index	m^2/m^2	0.0–9.5
	$STEM_A$	Stem reflectance variable range (for a fitted function)	–	0.0–1.0
	STEMFR	Stem fraction	–	0.0–1.0
	VGCF	Vegetation cover fraction: area covered by vegetation/total area of pixel	–	0.0–1.0
	C_{ab}	Leaf chlorophyll a + b content	$\mu g/cm^2$	0–80
	N	Leaf structure variable: measure of the internal structure of the leaf	–	1.0–4.5
	C_w	Leaf equivalent water thickness	cm	0.001–0.04
	C_m	Leaf dry matter content	g/cm^2	0.001–0.04
	C_{brown}	Leaf brown pigment content	–	0.00001–2
	LFINC	Mean leaf inclination angle	degree	10–89
	STINC	Mean stem inclination angle	degree	10–89
	LFHOT	Leaf BRDF variable: length of leaf/height of vegetation	m/m	0–0.9
	STHOT	Stem BRDF variable: length of stem/height of vegetation	m/m	0–0.9
Physical soil variables	$SOIL_A$	Soil profile variable: wetness of soil	–	0.0–1.0
	SOILCF	Soil cover fraction: area covered by soil/total area of pixel	–	0.0–1.0
Physical snow variables	$SNOW_A$	Snow profile variable: purity of snow	–	0.0–1.0
	SNOWCF	Snow cover fraction: area covered by snow/total area of pixel	–	0.0–1.0
Physical water body variables	$WaterBody_A$	Water body profile variable: purity of water	–	0.0–1.0
	WaterBodyCF	Water body cover fraction: area covered by water body/total area of pixel	–	0.0–1.0
Atmospheric condition variable	VIS	Diffuse/direct variable: scope of atmospheric clarity	km	50

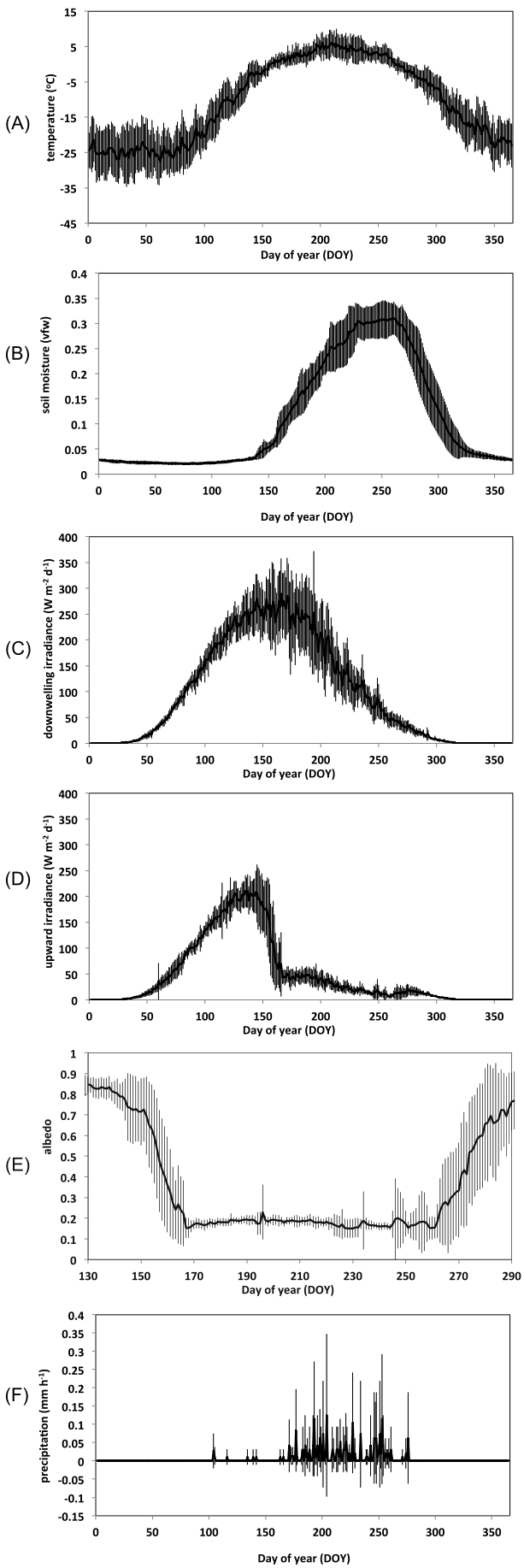

Fig. 2. (A) the 14-year-average daily temperature (°C) for 2001–2014; (B) the 12-year-average daily soil moisture (unit: volumetric fraction of water, vfw) for 2001–2012; (C) The 14-year-average daily downwelling irradiance (W m^{-2} d^{-1}) for 2001–2014; (D) the 14-year-average daily upward irradiance (W m^{-2} d^{-1}) for 2001–2014; (E) the 14-year-average daily albedo for 2001–2014; and (F) the 4-year-average daily precipitation (mm h^{-1}) for 2001–2004. Bars are standard deviations.

Table 2
Snowmelt dates determined with NOAA's ESRL method and from SNOWCF.

Year	NOAA Snowmelt Date (DOY)	Snowmelt Period from SNOWCF (DOY)
2001	162	161–184
2002	145	137–160
2003	155	153–168
2004	159	153–168
2005	166	161–168
2006	161	153–168
2007	157	153–160
2008	164	153–168
2009	158	153–168
2010	166	153–168
2011	157	153–168
2012	160	145–160
2013	153	145–160
2014	164	153–176

where n is the number of data points sampled according to Eq. (10) and Σ is the variance-covariance matrix of X. Σ is estimated by the usual sample variances and covariances in each step of the algorithm:

$$\Sigma_e = (S_{ij})_{p\times p}$$
$$S_{ij} = \frac{1}{n}\sum_{k=1}^{n}(x_{ki} - u_{ki})(x_{kj} - u_{kj})^{\ i,j = 1,\ \ldots,p} \tag{12}$$

The natural logarithm of the likelihood, the "log-likelihood" (*log (L)*), is used in the algorithm during its operation.

The algorithm defines the probability of accepting the new point as following:

$$Pr_{accept} = min\left(1, \frac{Pr(v_{new} \mid data)}{Pr(v_{old} \mid data)}\right) \tag{13}$$

If the algorithm accepts the new point, it will become the "old" point in next iteration; otherwise, the old point will still be the "old" point in the next iteration. To accelerate the speed of convergence of the Metropolis algorithm, we modified the adaptive algorithm as follows:

In each iteration, one variable is selected to change as

$$v_{new,s} = v_{old,s} + r \times (v_{max,s} - v_{min,s}) \tag{14}$$

where s = 1, …, 19, is the number of variables in the LVS3 model (see Table 1) that are allowed to search for solutions, *r* is randomly selected at each step between ± 0.5 · T_s, $v_{max,\ s}$ *and* $v_{min,\ s}$ are the maximum and minimum values allowed for the search, and T_s is the adaptive length parameter. If $v_{new,\ s}$ is accepted, then T_s is increased by a factor of 1.006569. If it is rejected, then T_s is decreased by a factor of 0.99. By changing the adaptive length parameters in this way, the T_s (*s* = 1, …, 19) of all variables are adjusted until varying any given variable leads to acceptance of about 23% to 44% of the time, which is considered an ideal acceptance rate for the Metropolis algorithm (Gelman et al., 2000). From the solution (the posterior distribution) of the variables in Table 1, we then obtain the solution of $fAPAR_{canopy}$, $fAPAR_{chl}$ and $fAPAR_{non\text{-}chl}$ with LVS3.

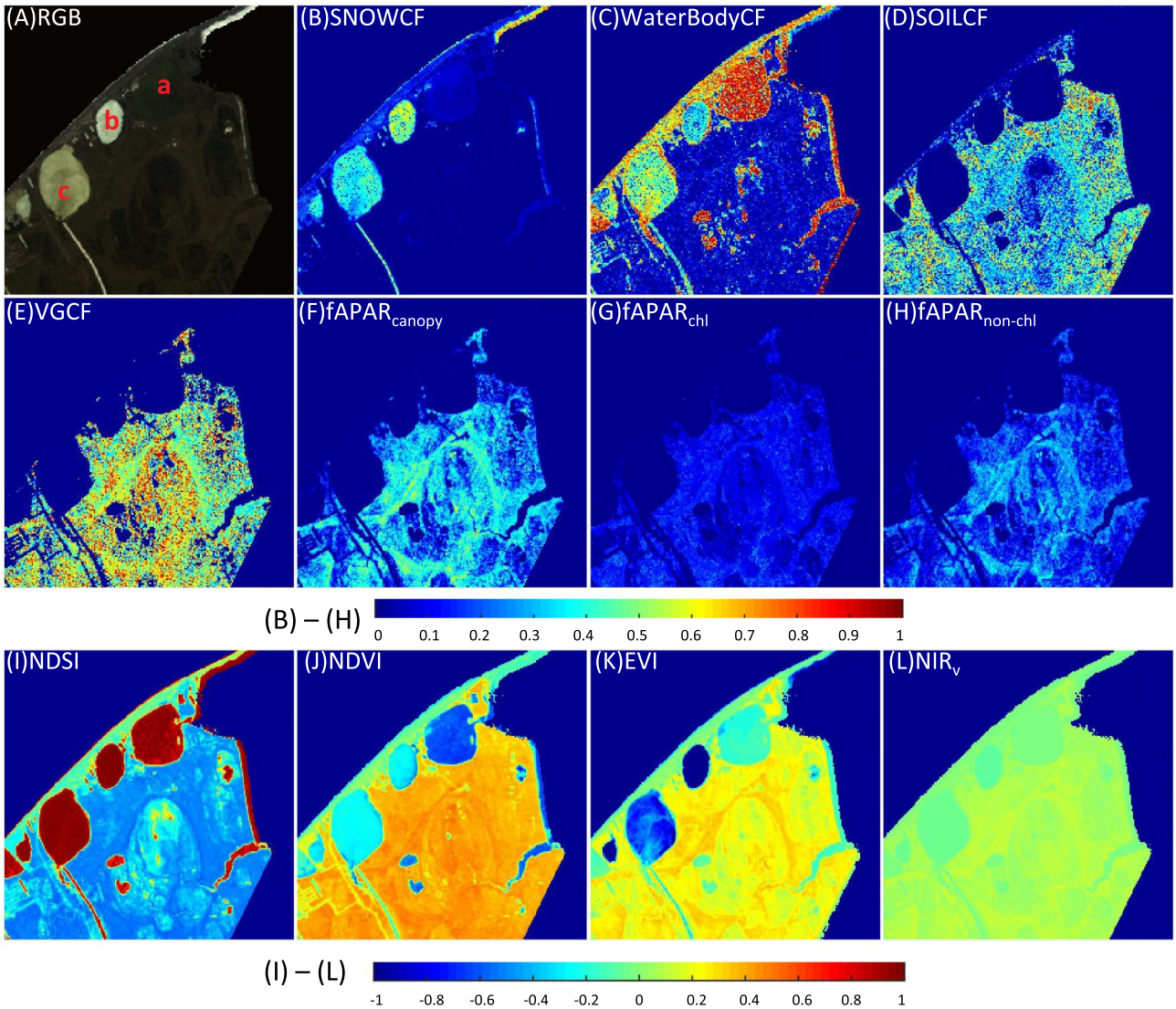

Fig. 3. The Arctic tundra at Utqiaġvik (formerly Barrow) in Alaska: (A) the true color image obtained by the EO-1 Hyperion on June 20, 2013 (DOY 171) at a spatial resolution of 30 m; and maps of (B) snow cover fraction (SNOWCF); (C) surface water cover fraction (WaterBodyCF); (D) soil cover fraction (SOILCF);(E) vegetation cover fraction (VGCF); (F) fAPAR$_{canopy}$; (G) fAPAR$_{chl}$; (H) fAPAR$_{non\text{-}chl}$; (I) NDSI; (J) NDVI; (K) EVI and (L) NIR$_v$. (B) – (H) share the upper legend describing values between 0 and 1, and (I) – (L) share the lower legend describing values between −1 and 1. Note that values of EVI less than −1 or > 1 are not shown. The North Salt Lagoon, the Imikpuk Lake, and the Middle Salt Lagoon are indicated as a, b, and c, respectively, in (A).

3. Results

3.1. Climate

Temperature and soil moisture have impacts on vegetation distribution, growth and phenology (Kelly and Goulden, 2008). Snow, snowmelt and precipitation have impacts on temperature and soil moisture. The multiyear-average daily air temperature increased from spring to DOY 208, and declined afterward toward winter (Fig. 2A). On average, air temperature was above 0 °C during DOYs 157–264 and below 0 °C between DOYs 265–156 of the next year. The multiyear-average daily soil moisture measured at 5 cm to 36 cm depth increased from spring to DOY 228, remained relatively constant during DOYs 229–260, and declined afterward toward winter (Fig. 2B). The NOAA ESRL method (Stone et al., 2002) determines snowmelt days with values of daily albedo computed with downwelling and upward irradiance measurements. The multiyear-average daily downwelling irradiance increased from spring to summer, was very variable in the spring and summer, and declined afterward toward winter (Fig. 2C). Average downwelling irradiances in green-up periods (DOYs 152–192), summertime periods (DOYs 200–248), and senescence periods (DOYs 256–280) during 2001–2014 were 257.32, 140.17, and 46.72 $Wm^{-2}d^{-1}$, respectively. Thus, downwelling irradiance values in these periods were 58%, 32% and 10%, respectively, of the value of total downwelling irradiance of entire growing season (DOYs 152–280). Snow has a higher albedo than water, soil or vegetation. Therefore, during the winter and early spring, upwelling irradiance increased directly with downwelling irradiance due to the presence of snow until DOY 135, then declined quickly during DOYs 136–167 with snowmelt (Fig. 2D). The multiyear-average daily albedo dropped quickly during

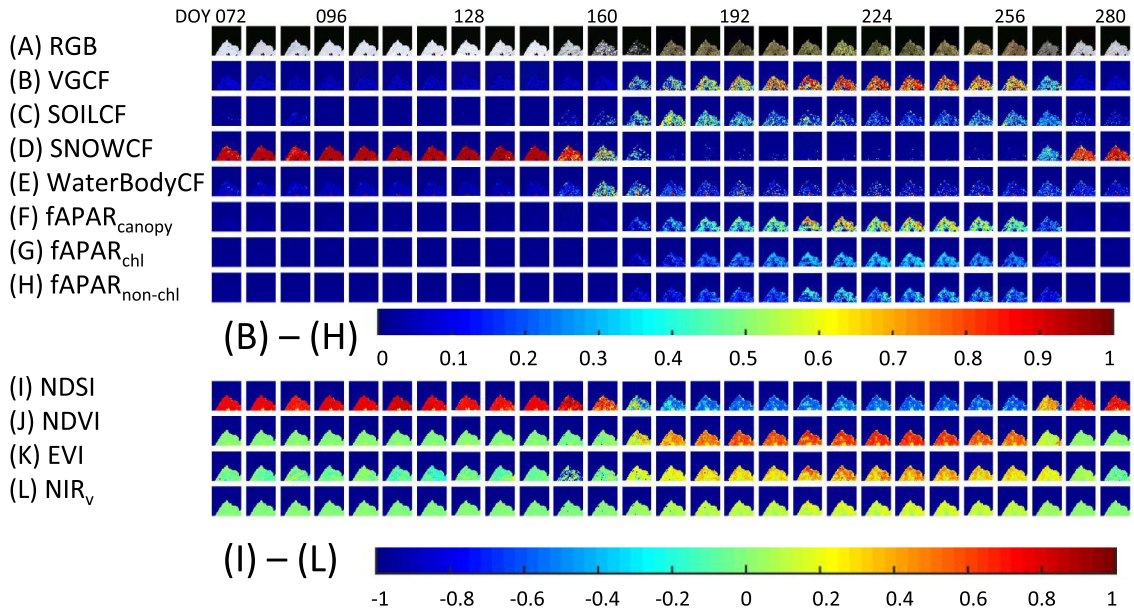

Fig. 4. The MODIS 8-day products for the 50 × 50 km^2 surrounding area of the US-Brw site in 2013: (A) RGB true color images; (B) VGCF; (C) SOILCF; (D) SNOWCF; (E) WaterBodyCF; (F) fAPAR$_{canopy}$; (G) fAPAR$_{chl}$; (H) fAPAR$_{non-chl}$; (I) NDSI; (J) NDVI; (K) EVI; and (L) NIR$_v$. (B) – (H) share the upper legend describing values between 0 and 1, and (I) – (L) share the lower legend describing values between −1 and 1. Note that values of EVI less than −1 or > 1 are not shown.

DOYs 141–167 from the highest values ~0.85, with significant year-to-year albedo differences during spring and early summer. The apparent ~90 day snow-free period was between DOYs 170 and 260 (Fig. 2E). Snowmelt days in 2001–2014 determined with the NOAA ESRL method were listed in Table 2, ranging between DOY 145–166 with the earliest snowmelt date in 2002. Precipitation mainly occurs during DOYs 161–275 (Fig. 2F). Environmental conditions in summer (temperature & soil moisture) are the most favorable for vegetation growth in this region.

3.2. Hyperion 30 m product maps

Snow, snowmelt, ponds and lakes are present simultaneously at the Utqiaġvik tundra area in green-up periods. A Hyperion subset of the region indicated in Fig. 1C from an image collected on June 20, 2013 (DOY 171) shows an example (Fig. 3). For the three water bodies in Utqiaġvik (as "a", "b", "c" indicated in Figs. 1C and 3A), snowmelt was fastest in the North Salt Lagoon ("a"), followed by the Middle Salt Lagoon ("c"), and the Imikpuk Lake ("b") was the slowest to melt (Fig. 3A–C). Fig. 3B–E maps the cover fractions of vegetation, soil, snow and water (SNOWCF, WaterBodyCF, SOILCF and VGCF), with mean values of 0.05, 0.26, 0.31 and 0.38, respectively. Fig. 3F–H maps fAPAR$_{canopy}$, fAPAR$_{chl}$ and fAPAR$_{non-chl}$, with mean values of 0.19, 0.07 and 0.12, respectively. The fAPAR$_{non-chl}$ in the early growing season was associated with standing non-green vegetation components left over from previous years and non-chlorophyll components of new leaves. The pixels with higher fAPAR$_{non-chl}$ contributions also were associated with areas having higher vegetation cover fractions (Fig. 3E vs. H). Fig. 3I–L manifests NDSI, NDVI, EVI and NIR$_v$. Mean values of NDVI, EVI and NIR$_v$ are 0.20, 0.11 and 0.03, respectively. Note that values of EVI less than −1 or > 1 are not shown in Fig. 3K. The RGB image and maps of SNOWCF, WaterBodyCF and NDSI (Fig. 3A, B, C and I) express that the NDSI has limited capacity to distinguish between surface water and snow, and its ability to quantitatively estimate SNOWCF is also limited. There are differences between the widely used NDVI and fAPAR$_{chl}$. The LVS3 model is coupled with the PROSPECT model, the SAIL model, the Soil model, the Snow model and the Surface water model (Section 2.4). We previously developed a coupled leaf-vegetation-soil radiative transfer model with the same models of PROSPECT, SAIL and Soil to describe pixels of vegetation, soil, or their mixtures, and have successfully applied it in forest and crop areas (Zhang et al., 2009, 2012, 2013, 2014a, 2015, 2016). The LVS3 model builds upon this leaf-vegetation-soil model and further considers snow and surface water. The North Salt Lagoon ("a"), the Middle Salt Lagoon ("c") and the Imikpuk Lake ("b") (Figs. 1C and 3A) do not contain vegetation or soil. They are prime areas to verify the LVS3 model. SOILCF and VGCF from the LVS3 model confirm that "a", "b" and "c" do not contain vegetation or soil (Fig. 3D–E), and the LVS3 model well distinguishes between snow and surface water (Fig. 3A–C) providing evidence of the correctness of the retrievals. These results support the feasibility of the physical model LVS3.

3.3. MODIS 500 m product maps

We used MODIS data to study the non-ocean area indicated in Fig. 1B for the years 2001–2014. Low illumination levels at the MODIS overpass times for dates before DOY 64 or after DOY 288 for this region (Fig. 2C) result in poor data quality. Therefore, we only present results for DOYs 72–280. The cover fractions (VGCF, SOILCF, SNOWCF, and WaterBodyCF), and the fAPAR parameters (fAPAR$_{canopy}$, fAPAR$_{chl}$ and fAPAR$_{non-chl}$) were retrieved from the LVS3 model with the 8-day MODIS surface reflectance products obtained from the MAIAC procedure (see Section 2.2) and the Metropolis approach (see Section 2.4). Values for NDSI, NDVI, EVI, EVI2 and NIR$_v$ were computed from the same MODIS surface reflectance products. Satellite remote sensing products of vegetation, soil, snow and surface water from MODIS in 2013 were presented in Fig. 4, expressing temporal and spatial dynamics of the tundra ecosystem. NDSI, NDVI, EVI and NIR$_v$ ranged −0.97 to 0.99, −0.65 to 0.85, −6.94 to 15.4, and − 0.07 to 0.38, respectively. Note that, values for EVI less than −1 or > 1 are not shown in Fig. 4K.

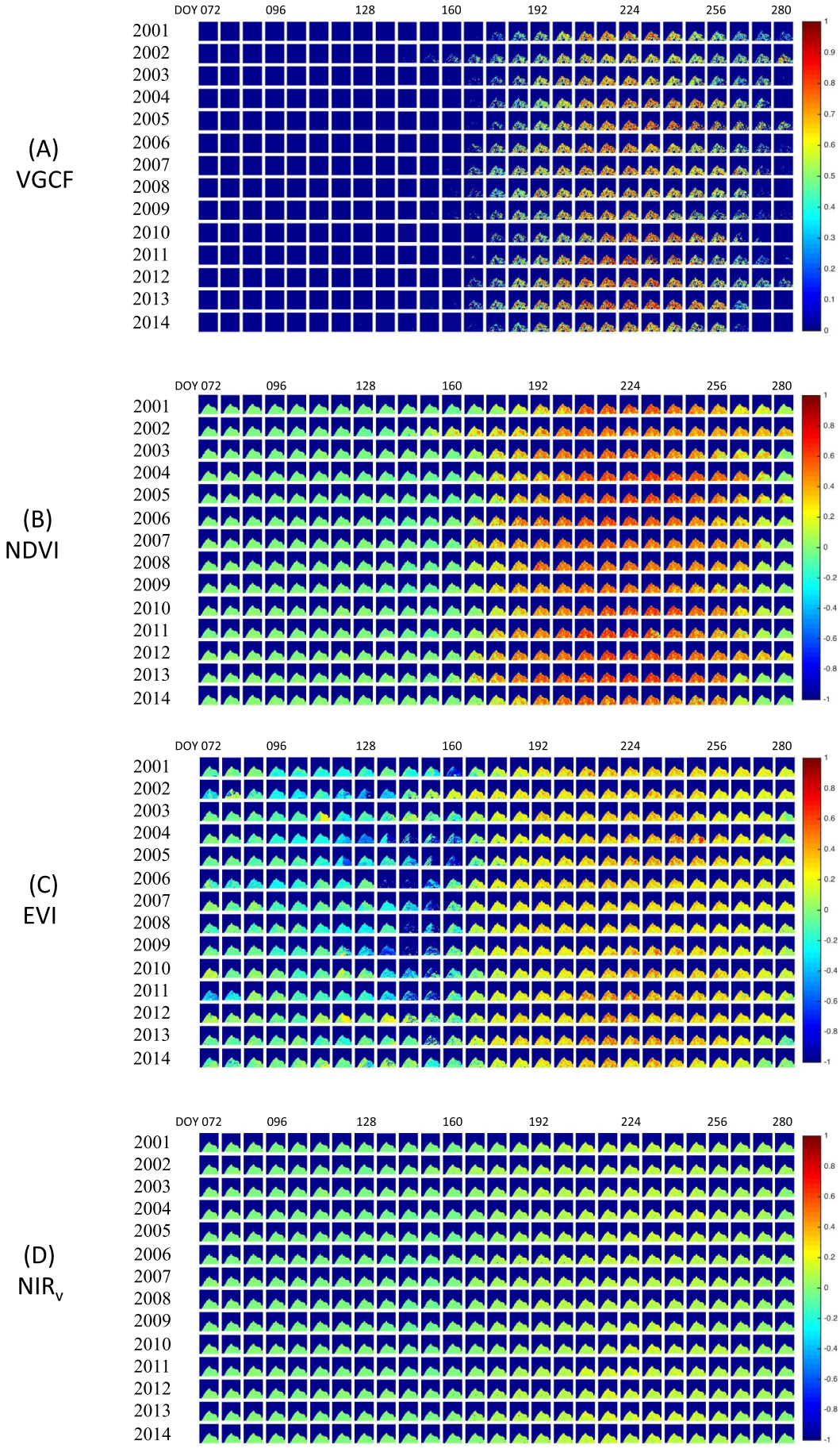

(caption on next page)

Fig. 5. MODIS seasonal vegetation products for the 50 × 50 km^2 surrounding area of the US-Brw site in 2001–2014: maps of (A) VGCF; (B) NDVI; (C) EVI; (D) NIR_v; (E) $fAPAR_{canopy}$; (F) $fAPAR_{chl}$; and (G) $fAPAR_{non\text{-}chl}$, and time series of (H) VGCF, $fAPAR_{canopy}$, $fAPAR_{chl}$, and $fAPAR_{non\text{-}chl}$, and (I) VGCF, NDVI, EVI2 and NIR_v.

3.3.1. Spatial and temporal patterns of vegetation

Fig. 5 displays maps of the four biophysical variables (VGCF, $fAPAR_{canopy}$, $fAPAR_{chl}$, and $fAPAR_{non\text{-}chl}$) and three empirical spectral indices (NDVI, EVI and NIR_v) describing spatial and temporal vegetation patterns for the years 2001–2014. Each row in Fig. 5A–G shows 8-day values throughout a year. The biophysical variables VGCF (Fig. 5A), $fAPAR_{canopy}$ (Fig. 5E), $fAPAR_{chl}$ (Fig. 5F) and $fAPAR_{non\text{-}chl}$ (Fig. 5G) have valid values that fall between 0 and 1. These biophysical products are compared with the empirical indices NDVI (Fig. 5B), EVI (Fig. 5C), and NIR_v (Fig. 5D). NDVI and NIR_v had negative values in spring/winters that are not shown in Fig. 5B and D. EVI had negative values and values greater than one in snow seasons that are not shown in Fig. 5C. On multiple times (DOY 112 of 2003, DOY 120 of 2012, and DOY 136 of 2012), EVI had positive values (Fig. 5C) while there was no vegetation viewable from space (Fig. 5A).

Fig. 5H–I shows 2-D plots for the 8-day seasonal time series over fourteen years (2001–2014) for the 7 variables (VGCF, $fAPAR_{canopy}$, $fAPAR_{chl}$, $fAPAR_{non\text{-}chl}$, NDVI, EVI2 and NIR_v). The VGCF (Fig. 5H) attained the highest fractional estimates (0.575–0.733) among all the vegetation biophysical variables and empirical indices. At the end of snow/snowmelt season in each year, the VGCF increased as vegetation grew and spatially expanded, reaching annual maximum values, declining afterward. The $fAPAR_{canopy}$ variable attained lower values in summers than VGCF, ranging between 0.376 and 0.539. In summertime periods (DOYs 200–248), both chlorophyll and non-chlorophyll components ($fAPAR_{chl}$ and $fAPAR_{non\text{-}chl}$) significantly contributed to $fAPAR_{canopy}$. Annual peak values of NDVI were lower than those of the VGCF, but higher than those of $fAPAR_{canopy}$ (Fig. 5H–I), between 0.488 and 0.631. Annual peak values of NDVI were almost twice as high as EVI2. Summertime EVI2 values were higher than those for $fAPAR_{chl}$; summertime NIR_v values were lower than those obtained for $fAPAR_{chl}$ and $fAPAR_{non\text{-}chl}$.

3.3.2. Spatial and temporal patterns of soil

At the beginning of the green-up periods, snow melts, bare soil and surface water from snowmelt are viewable from MODIS. While in the senescence periods, after a snow event, snow will cover the landscape and less soil and vegetation will be viewable from MODIS. Maps of the physical variable SOILCF over this study area during 2001–2014 are presented in Fig. 6A, showing the spatial and temporal patterns for SOILCF. Fig. 6B shows these 8-day values in a time series for SOILCF along with the NDVI, expressing how NDVI changed with SOILCF seasonally and inter-annually. Note that because of vegetation growth and expansion in summer, the temporal change in SOILCF has an "M" shape, with peaks in the green-up and senescence periods and a mid-summer depression.

3.3.3. Spatial and temporal patterns of snow

Maps for the physical variable SNOWCF and the empirical index NDSI during 2001–2014 are presented in Fig. 7A–B showing the spatial and temporal patterns of snow. The long fall–spring snow season is clearly expressed. Fig. 7C shows the time series of 8-day SNOWCF, NDVI and NDSI, expressing how NDVI and NDSI changed with SNOWCF seasonally and inter-annually. Values of NDSI in summer were negative (not shown in Fig. 7B). The NDVI increased when snow was gone. Fig. 7 indicates that it is a challenge to accurately estimate SNOWCF with NDSI.

3.3.4. Spatial and temporal patterns of surface water

Surface water bodies include lakes, ponds, snowmelt, etc. Maps of the physical variable WaterBodyCF during 2001–2014 are presented in Fig. 8A, showing the spatial and temporal patterns of surface water. Snowmelt in 2002 occurred on the earliest date and resulted in the longest snow-free spring-summer time among the 14 years. Fig. 8B shows the seasonal time series of SNOWCF, WaterBodyCF and NDVI, expressing how NDVI changed with WaterBodyCF and SNOWCF seasonally and inter-annually. WaterBodyCF in Fig. 8B had an anchor shape with a peak in the springtime following rapid snowmelt when there is very little new vegetation, so more bare soil and water bodies are viewable (i.e., increases in SOILCF and WaterBodyCF) (see Figs. 6 and 8). This seasonal peak in surface water coverage occurred between DOYs 144 and 168. Moving into summer, vegetation growth increased as shown by VGCF while bare soil and surface water cover decreased (i.e., decreases in SOILCF and WaterBodyCF).

4. Discussion

The radiative transfer model used to produce MOD15A2 FPAR (Myneni et al., 2002; Wang, 2002), the "GLASS leaf area index" based $fAPAR_{canopy}$ algorithm (Xiao et al., 2015), the $fAPAR_{canopy}$ algorithm developed by Chen for boreal conifer forests (Chen, 1996), the $fAPAR_{canopy}$ algorithm developed for the Medium Resolution Imaging Spectrometer (MERIS) (Gobron et al., 2008), and the leaf-canopy-soil coupled radiative transfer model PROSAIL2 (Zhang et al., 2009, 2012, 2013, 2014a, 2015, 2016), are designed for pixels of vegetation, soil, or their mixtures (Tao et al., 2015). The LVS3 model considers vegetation, soil, snow, surface water, and their mixtures, which distinguishes well between chlorophyll, non-chlorophyll components of vegetation, soil, snow and surface water. For the study region indicated in Fig. 1B, we show how the NDVI, VGCF, SOILCF, SNOWCF and WaterBodyCF variables changed seasonally and inter-annually during 2001–2014 (Figs. 5I, 6B, 7C and 8B). One interesting question is: how do the empirical indices change in response to cover variations of vegetation, soil, snow and surface water? Fig. 9 shows how the five remote sensing empirical indices (NDVI, EVI, NIR_v, EVI2, and NDSI) are affected by VGCF, SOILCF, SNOWCF, WaterBodyCF. Fig. 9A expresses how the NDVI changes with these cover fractions during 2001–2014. Over the mid-summer periods (when NDVI > 0.3), the NDVI increased along with increases for the VGCF and with decreases for the WaterBodyCF, and SOILCF. Over the green-up and senescence periods (when NDVI < 0.3), the NDVI increased with increases for both the SOILCF and the VGCF and with a decrease for the SNOWCF, while the relationship between the NDVI and WaterBodyCF is complicated since the NDVI increases from inundation stage to non-inundation stage. Fig. 9B shows the relationships between EVI and VGCF, SOILCF, SNOWCF, WaterBodyCF during 2001–2014. Note that EVI values that fell out of range between −0.2 and 0.8 are not shown. Fig. 9C–E shows the relationships between NIR_v, EVI2, and NDSI with the cover fractions (VGCF, SOILCF, SNOWCF, WaterBodyCF).

As expected, NDVI, EVI, EVI2 and NIR_v increased in concert with increasing VGCF values, and the NDSI increased with SNOWCF (non-linearly). Among NDVI, EVI2 and NIR_v, NDVI increased the greatest with VGCF (NDVI = 1.031 × VGCF - 0.118; EVI2 = 0.536 × VGCF - 0.067; NIR_v = 0.233 × VGCF - 0.034). However, soil, snow and surface water also affected these vegetation spectral indices (NDVI, EVI, EVI2 and NIR_v). NDVI, EVI2 and NIR_v decreased with SNOWCF, and NDVI

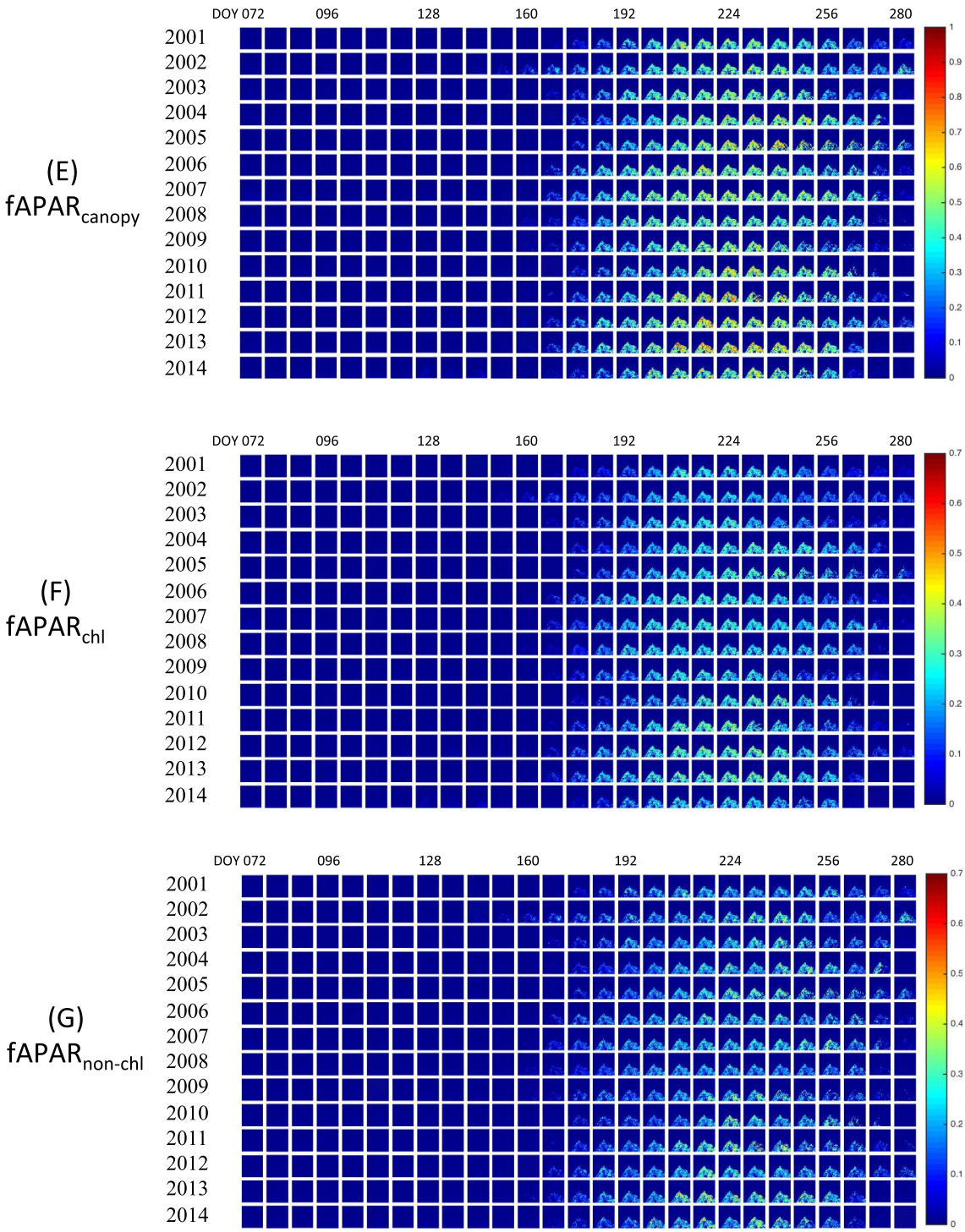

Fig. 5. (*continued*)

changed the greatest with SNOWCF among the three indices [NDVI = −0.124 × ln(SNOWCF) - 0.050; EVI2 = −0.062 × ln (SNOWCF) - 0.027; NIR_v = −0.027 × ln(SNOWCF) - 0.016]. When VGCF > 0.4, EVI increased with VGCF and decreased with SNOWCF; when VGCF was low and SNOWCF was high, EVI changed from very low values to very high values. Surface water, soil, and vegetation also affected NDSI. NDSI decreased with VGCF (NDSI = −2.474 × VGCF +0.925). These findings are also supported by other studies (e.g., Chang et al., 2019; Huete et al., 2002; Luus et al., 2017; Lv and Pomeroy, 2019; Walther et al., 2016). NDSI was highly correlated with sum of SNOWCF and WaterBodyCF (Fig. 9F, sum = 0.5893 × NDSI +0.4342, R^2 = 0.976). The NIR_v has a narrower range than the NDVI, and the EVI2 has a narrower range than the EVI. Vegetation in this study area is often a mixture of vascular and non-vascular plants. It is challenging to interpret vegetation signal with NDVI and EVI for pixels mixed with snow/snowmelt, or to interpret snow signal with NDSI for pixels mixed with vegetation/snowmelt/soil (Chang et al., 2019; Lv and Pomeroy, 2019; Moulin et al., 1997; Walther et al., 2016). VGCF, $fAPAR_{chl}$, $fAPAR_{non\text{-}chl}$ and $fAPAR_{canopy}$ from LVS3 provide alternatives for vegetation monitoring, and SNOWCF from LVS3 provides

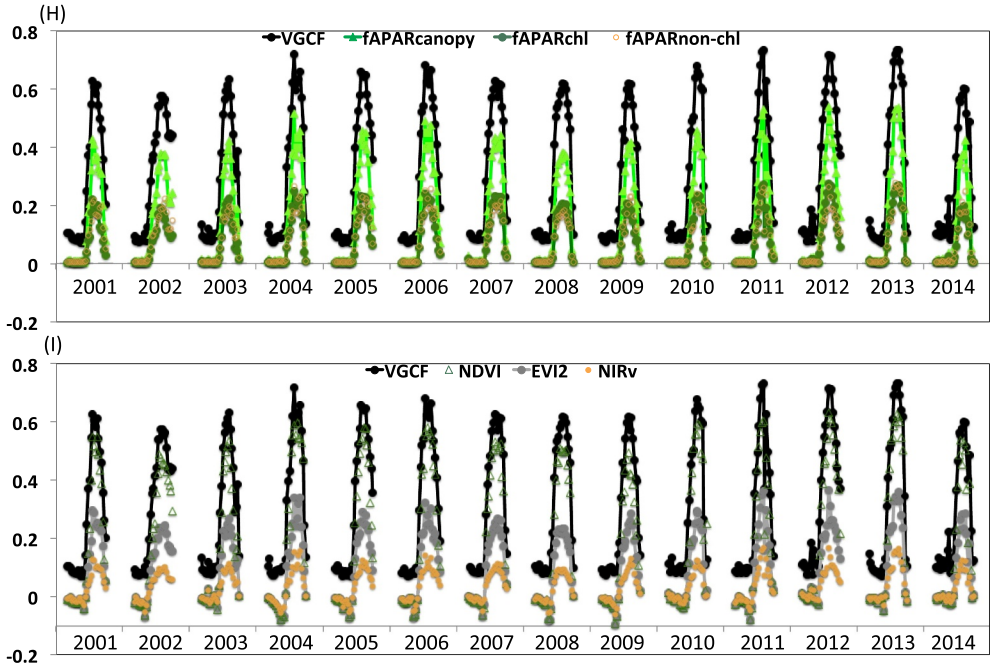

Fig. 5. (*continued*)

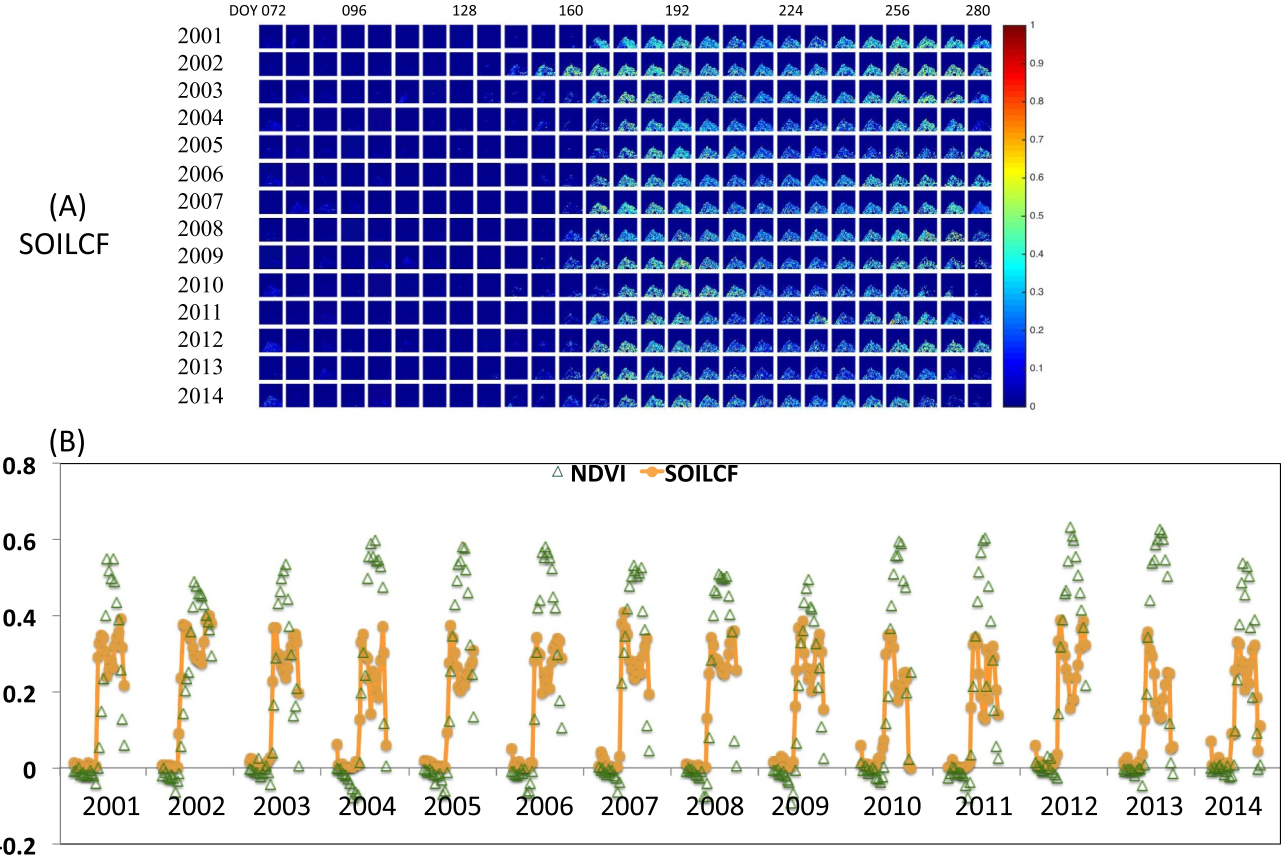

Fig. 6. (A) MODIS seasonal maps of SOILCF for the 50 × 50 km^2 surrounding area of the US-Brw site in 2001–2014; and (B) seasonal time series for the NDVI and SOILCF.

alternative for snow monitoring.

For the study area indicated in Fig. 1B, the NDVI seasonal anomalies are substantially different from the seasonal anomalies of VGCF, fAPAR$_{chl}$, and fAPAR$_{non\text{-}chl}$ (Fig. 10). Magnitudes of the fAPAR$_{chl}$ and fAPAR$_{non\text{-}chl}$ anomalies were less than those of the NDVI and VGCF anomalies. The NDVI anomalies in some periods (green-up period of 2001, summer of 2009, senescence of 2003, senescence of 2011, and senescence of 2014) and the VGCF anomaly in senescence of 2014 were

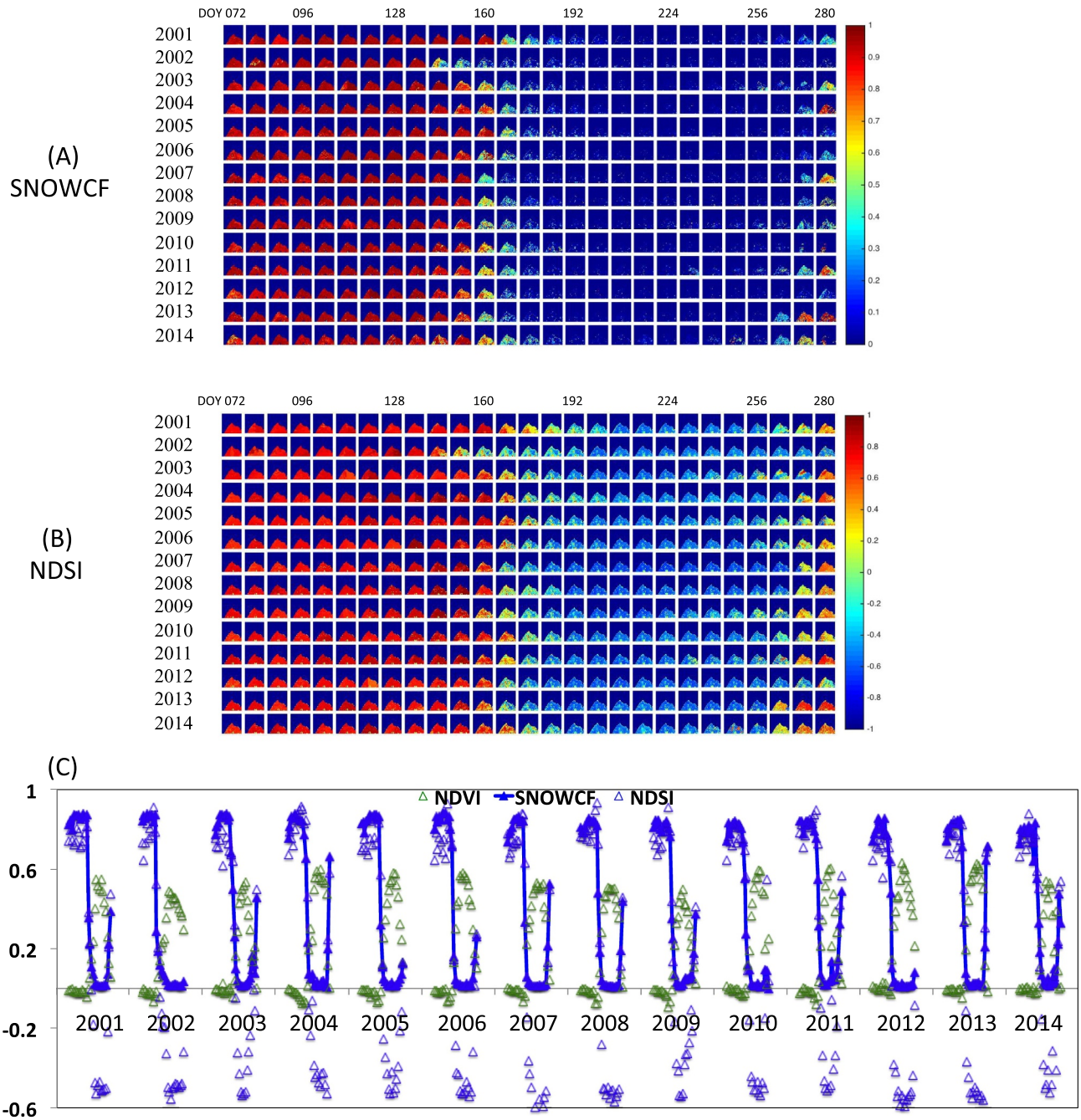

Fig. 7. (A) MODIS seasonal maps of SNOWCF for the 50 × 50 km^2 surrounding area of the US-Brw site in 2001–2014; (B) MODIS seasonal maps of NDSI; and (C) seasonal time series for the NDVI, SNOWCF and NDSI.

well below other anomalies. The NDVI anomalies in some other periods (green-up period of 2013, summer of 2013, senescence of 2002, and senescence of 2012) and the VGCF anomaly in summer of 2013 were the highest among all the anomalies in Fig. 10. The seasonal NDVI anomalies may be enhanced due to changes in seasonal water, soil, or snow cover. Tundra gross primary productivity (GPP) is a function of the product of $fAPAR_{chl}$ and incident PAR ($APAR_{chl} = fAPAR_{chl} \times PAR$). We assumed 50% of shortwave radiation in Utqiaġvik was in the PAR spectral interval (Frouin and Pinker, 1995; Pinker and Laszlo, 1992; Pinker et al., 2010). Note that, contrary to mid-latitudes, the springtime PAR values were higher than summer and fall PAR values. Magnitudes of anomalies of green-up total $APAR_{chl}$ and anomalies of summer total $APAR_{chl}$ were greater than that of senescence total $APAR_{chl}$ (Fig. 11). Therefore, the $fAPAR_{chl}$ anomalies in

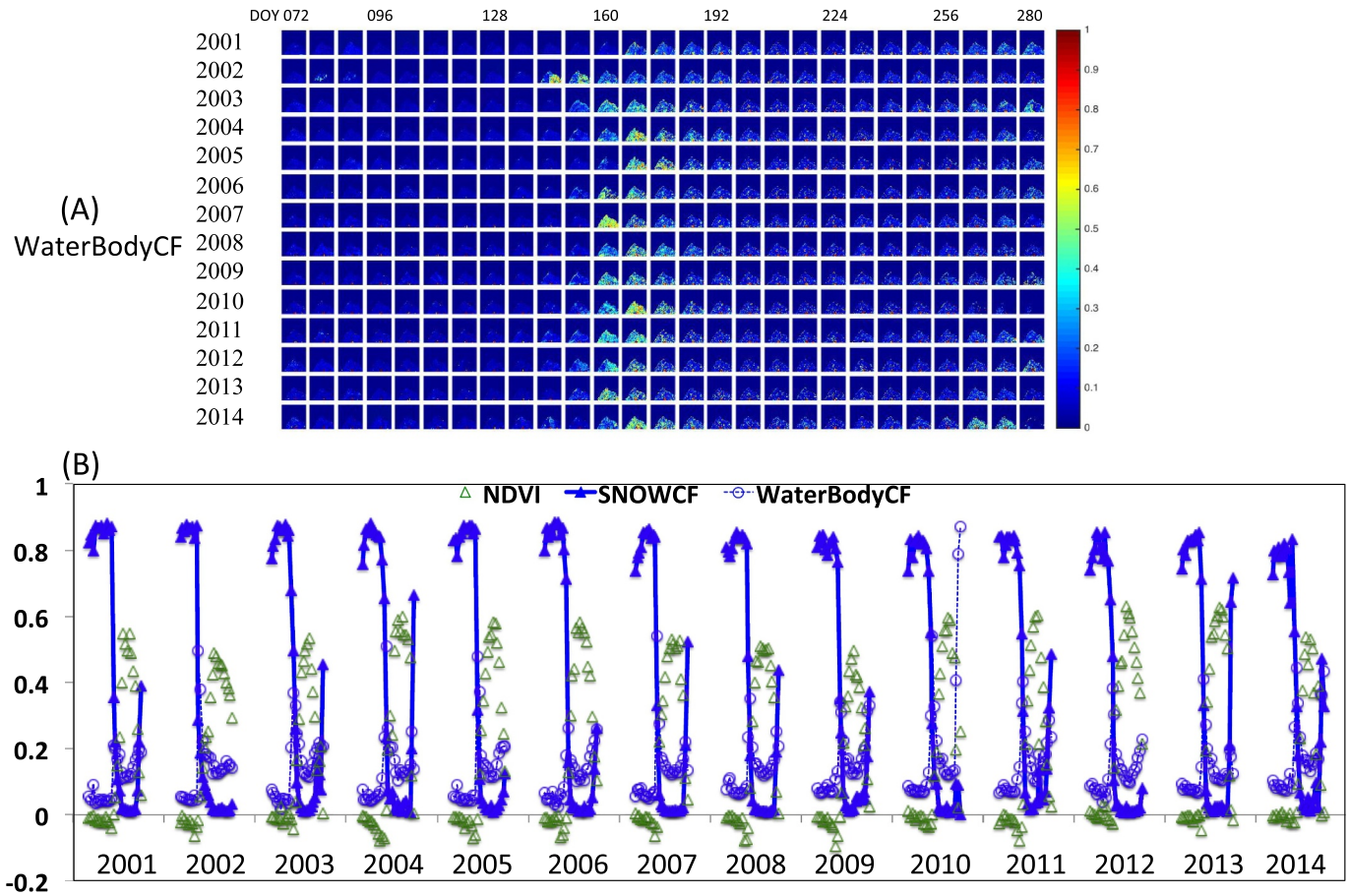

Fig. 8. (A) MODIS seasonal maps of WaterBodyCF for the 50 × 50 km^2 surrounding area of the US-Brw site in 2001–2014; and (B) seasonal time series for the NDVI, SNOWCF and WaterBodyCF.

green-up and summertime periods have more impacts on tundra GPP than its anomalies in senescence periods.

Retrieval of $fAPAR_{chl}$ from the LVS3 physical model will be very beneficial for estimation of yield of solar induced fluorescence (SIF_{yield}) (Li et al., 2018; Tagliabue et al., 2019; van der Tol et al., 2009a, 2014; Yang et al., 2018; Zhang et al., 2018b), simulation of GPP (Croft et al., 2013; Dong et al., 2015; Gamon et al., 2013; Huemmrich et al., 2010; Liang et al., 2012; Luus et al., 2017; Sims et al., 2008; Tagliabue et al., 2019; van der Tol et al., 2009b; Waring et al., 2016; Xiao et al., 2004b; Zhang et al., 2014a; Zhao and Running, 2010), and phenology studies with observations mixed with soil, snow, and/or snowmelt (Chang et al., 2019; Gao et al., 2017; Zhang et al., 2003). VGCF and SOILCF retrieved with the LVS3 model provide inputs for evapotranspiration modeling (Anderson et al., 2011; Fisher et al., 2017; Yang et al., 2017). SNOWCF derived with the LVS3 model will be valuable for snow cover extent studies, especially for observations mixed with forest, snow and snowmelt (Lv and Pomeroy, 2019; Salminen et al., 2009; Zhou et al., 2013). Land cover changes caused by fire may be detected with decreases of VGCF, $fAPAR_{chl}$, $fAPAR_{non\text{-}chl}$ and $fAPAR_{canopy}$, and land cover changes due to flooding may be detected with increases of WaterBodyCF (Zhan et al., 2002). Other disturbance monitoring may also benefit from retrievals from the LVS3 model (Tang et al., 2019).

Radiative transfer models including the LVS3 model often have many variables (e.g., Baret and Fourty, 1997; Chen, 1996; Fang et al., 2019; Gobron et al., 2008; Jacquemoud and Baret, 1990; Jacquemoud et al., 2009; Myneni et al., 2002; Tao et al., 2015; Verhoef, 1984, 1985; Wang, 2002; Xiao et al., 2015; Zhang et al., 2009, 2016), and they are possibly influenced by biases in the quantitative estimation of the variables of interest. In-situ data at the remote study area in Utqiaġvik during the study period for validation of the LVS3 model are very limited. Additional validation activities relying on availability of funding, manpower and facility in future will be valuable. We will explore the applicability of the LVS3 model in the entire Arctic and Boreal region and other regions that are covered by snow/snowmelt in winter/spring.

5. Conclusions

MODIS observations of the Utqiaġvik tundra ecosystem in Alaska often consist of vascular and non-vascular plants, soil, surface water bodies and/or snow. In this work, the variability of empirical indices (NDVI, EVI, NIR_v, EVI2, NDSI) in response to changes of cover fractions of vegetation, soil, snow and surface water (VGCF, SOILCF, SNOWCF, WaterBodyCF) was investigated with MODIS images and the LVS3 model. The vegetation indices (NDVI, EVI, EVI2 and NIR_v) differ from VGCF, $fAPAR_{chl}$, $fAPAR_{non\text{-}chl}$, and $fAPAR_{canopy}$. NDVI, EVI2 and NIR_v linearly increase with VGCF. EVI linearly increases with VGCF when VGCF > 0.3 while there is no clear linear or non-linear correlation

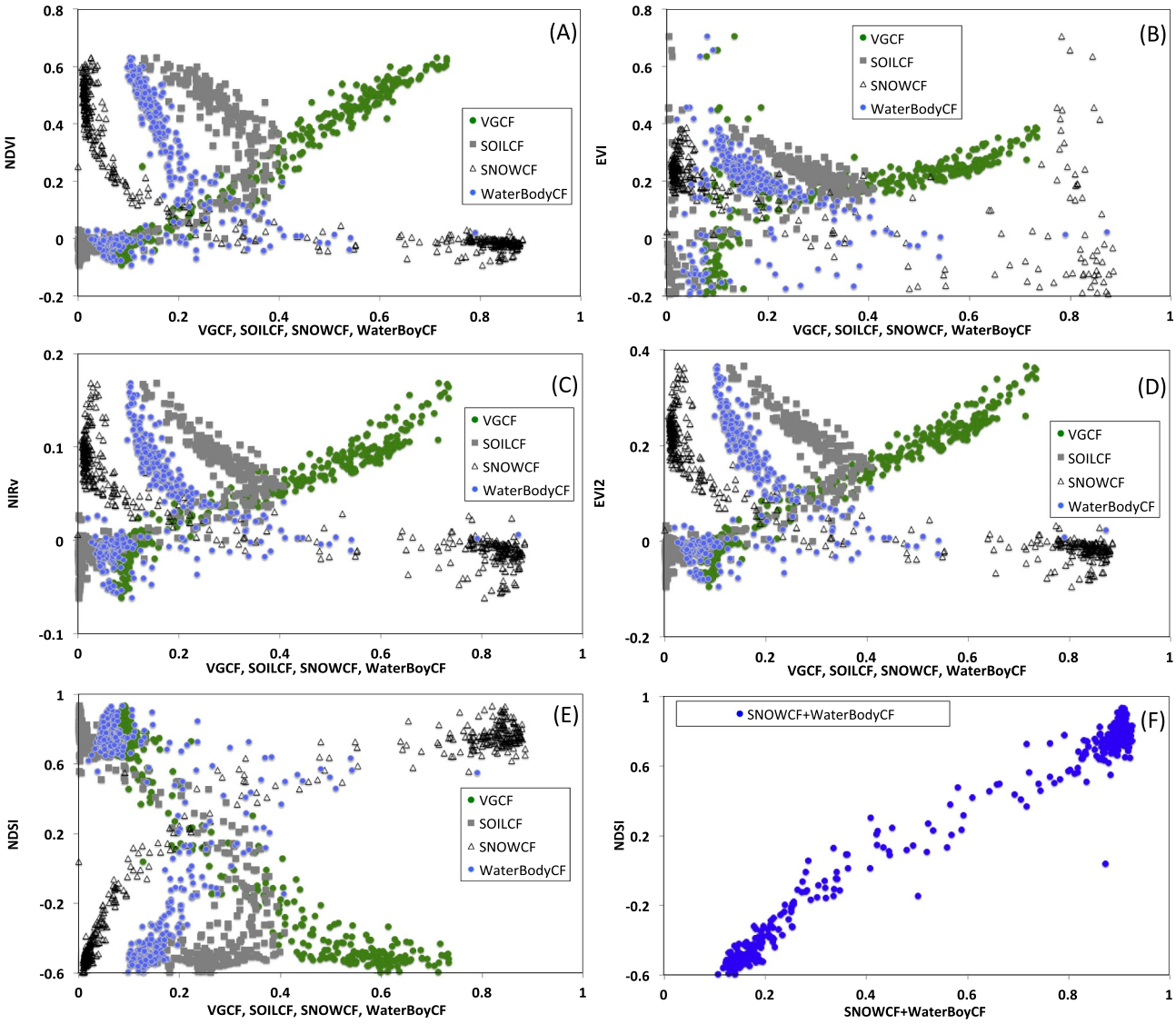

Fig. 9. Relationships between empirical indices and physical variables VGCF, SOILCF, SNOWCF and WaterBodyCF for the 50 × 50 km^2 surrounding area of the US-Brw site in 2001–2014: (A) NDVI; (B) EVI; (C) NIR_v; (D) EVI2 and (E) NDSI.

between EVI and VGCF when VGCF ≤0.3. EVI2 performs better than EVI on prediction of VGCF for this area. Presence of snow makes lower the observed values of NDVI, EVI2 and NIR_v. The relationship between EVI and snow is complicated. After snowmelt is gone, all the vegetation indices (NDVI, EVI, EVI2 and NIR_v) linearly decrease with SOILCF and WaterBodyCF, and WaterBodyCF has stronger impacts on vegetation indices than SOILCF. NDSI non-linearly increases with SNOWCF, but linearly increases with sum of SNOWCF and WaterBodyCF (sum = 0.5893 × NDSI + 0.4342, R^2 = 0.976). NDSI linearly decreases with VGCF, and the relationship between NDSI and SOILCF is complex.

The circumpolar high latitude region is most susceptible to current climate changes causing increasingly higher annual surface temperatures. We demonstrate that the satellite remote sensing approaches in use to document the surface changes, especially those that are largely dependent on NDVI, may not provide the most accurate information to correctly diagnose ecosystem productivity trends in this critical environmental zone. On average over the fourteen summer periods, the $fAPAR_{chl}$ and $fAPAR_{non\text{-}chl}$ variables contributed approximately half each to $fAPAR_{canopy}$ (51% versus 49%). Retrievals of VGCF, $fAPAR_{canopy}$, $fAPAR_{chl}$ and $fAPAR_{non\text{-}chl}$ from the LVS3 model are alternatives for vegetation monitoring and have the potential to be integrated into studies of plant physiology, vegetation phenology, ecological modeling, agriculture, carbon cycle modeling, hydrological modeling and climate.

CRediT authorship contribution statement

Qingyuan Zhang: Conceptualization, Methodology, Software, Formal analysis, Writing - original draft. **Tian Yao:** Formal analysis, Visualization, Writing - review & editing. **K. Fred Huemmrich:** Formal analysis, Writing - review & editing. **Elizabeth M. Middleton:** Writing - review & editing. **Alexei Lyapustin:** Software, Writing - review & editing. **Yujie Wang:** Software, Writing - review & editing.

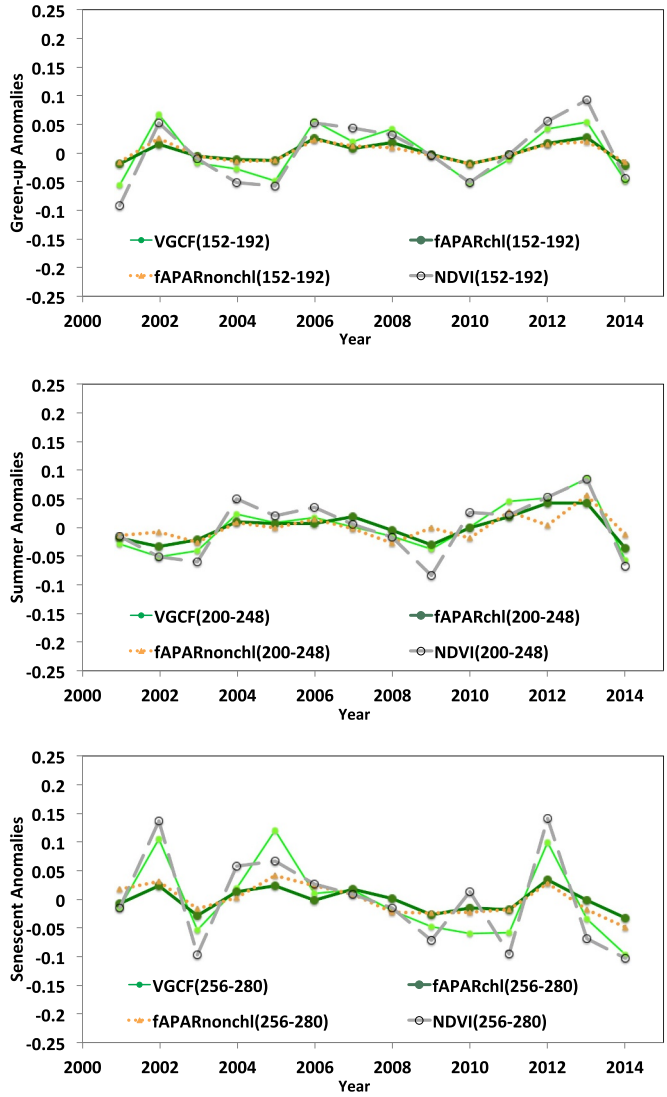

Fig. 10. Anomalies of seasonal VGCF, $fAPAR_{chl}$, $fAPAR_{non\text{-}chl}$ and NDVI for the 50 × 50 km^2 surrounding area of the US-Brw site in 2001–2014: (A) Green-up Anomalies; (B) Summer Anomalies; and (C) Senescent Anomalies. (For interpretation of the references to color in this figure legend, the reader is referred to the web version of this article.)

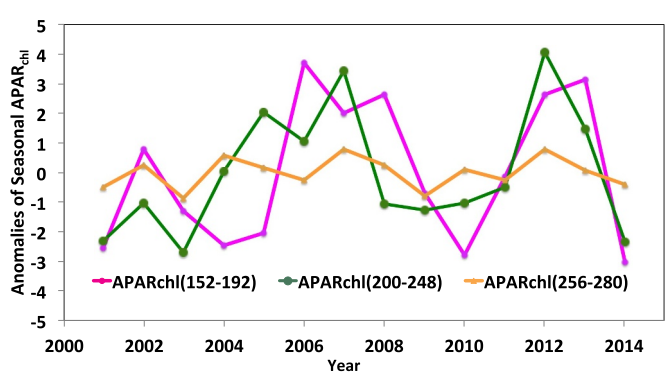

Fig. 11. Anomalies of seasonal total $APAR_{chl}$ for the 50 × 50 km^2 surrounding area of the US-Brw site in 2001–2014.

Acknowledgments

We thank two anonymous reviewers for their constructive comments and suggestions on the earlier version of the manuscript. We also thank Dr. Maosheng Zhao for providing suggestions of relationship between PAR and downwelling shortwave radiation. This work was partially funded by the NASA Terrestrial Ecology Program (Grant # NNX12AJ51G, PI: Q. Zhang) and the Science of Terra and Aqua Program (Grant # NNX14AK50G, PI: Q. Zhang). K. F. Huemmrich was supported by ABoVE project grants NNX15AT78A and NNX17AC58A. This study was also partially supported by two NASA Headquarters sponsored programs (PI: E. Middleton), the Earth Observing One (EO-1) Mission Science Office (Sponsor, Dr. Garik Gutman) and the Surface Biology and Geology (SBG) science support project at the Goddard Space Flight Center (NASA/GSFC) through Mr. William (Woody) Turner. Computational support and resources were provided by the NASA Center for Climate Simulation (NCCS) at Goddard Space Flight Center and the NASA High-End Computing (HEC) Program through the NASA Advanced Supercomputing (NAS) Division at Ames Research Center.

Declaration of competing interest

The authors declare that they have no known competing financial interests or personal relationships that could have appeared to influence the work reported in this paper.

References

ACIA, 2004. Arctic climate impact assessment. In: Impacts of a Warming Arctic, pp. 146.
Anderson, M., Kustas, W.P., Norman, J.M., Hain, C.R., Mecikalski, J.R., Schultz, L., Gonzalez-Dugo, M.P.G., Cammalleri, C., d'Urso, G., Pimstein, A., Gao, F., 2011. Mapping daily evapotranspiration at field to continental scales using geostationary and polar orbiting satellite imagery. Hydrol. Earth Syst. Sci. 15, 223–239.
Andrieu, B., Baret, F., Jacquemoud, S., Malthus, T., Steven, M., 1997. Evaluation of an improved version of SAIL model for simulating bidirectional reflectance of sugar beet canopies. Remote Sens. Environ. 60, 247–257.
Badgley, G., Field, C.B., Berry, J.A., 2017. Canopy near-infrared reflectance and terrestrial photosynthesis. Sci. Adv. 3, e1602244.
Badhwar, G.D., Verhoef, W., Bunnik, N.J.J., 1985. Comparative-study of SUITS and SAIL canopy reflectance models. Remote Sens. Environ. 17, 179–195.
Baret, F., Fourty, T., 1997. Radiometric estimates of nitrogen status in leaves and canopies. In: Lemaire, G. (Ed.), Diagnosis of the Nitrogen Status in Crops. Springer, Berlin, pp. 201–227.
Barry, P.S., Mendenhall, J., Jarecke, P., Folkman, M., Pearlman, J., Markham, B., 2002. EO-1 hyperion hyperspectral aggregation and comparison with EO-1 advanced land imager and Landsat 7 ETM+. In: *IEEE International Geoscience and Remote Sensing Symposium (IGARSS)* Toronto Canada.
Braswell, B.H., Sacks, W.J., Linder, E., Schimel, D.S., 2005. Estimating diurnal to annual ecosystem parameters by synthesis of a carbon flux model with Eddy covariance net ecosystem exchange observations. Glob. Chang. Biol. 11, 335–355.
Brown, J., Everett, K.R., Webber, P.J., S. F. MacLean, J., Murray, D.F., 1980. An Arctic Ecosystem: The Coastal Tundra at Barrow, Alaska. Ross, Inc, Dowden, Hutchingon.
Carroll, M., Loboda, T., 2017. Multi-decadal surface water dynamics in North American tundra. Remote Sens. 9, 497–512.
Carroll, M.L., DiMiceli, C.M., Townshend, J.R.G., Sohlberg, R.A., Elders, A.I., Devadiga, S., Sayer, A.M., Levy, R.C., 2016. Development of an operational land water mask for MODIS collection 6, and influence on downstream data products. Int. J. Digital Earth 10, 207–218.
Chang, Q., Xiao, X., Jiao, W., Wu, X., Doughty, R., Wang, J., Du, L., Zou, Z., Qin, Y., 2019. Assessing consistency of spring phenology of snow-covered forests as estimated by vegetation indices, gross primary production, and solar-induced chlorophyll fluorescence. Agric. For. Meteorol. 275, 305–316.
Chen, J.M., 1996. Canopy architecture and remote sensing of the fraction of photosynthetically active radiation absorbed by boreal conifer forests. IEEE Trans. Geosci. Remote Sens. 34, 1353–1368.
Cheng, Y.-B., Zhang, Q., Lyapustin, A.I., Wang, Y., Middleton, E.M., 2014. Impacts of light use efficiency and fPAR parameterization on gross primary production modeling. Agric. For. Meteorol. 189–190, 187–197.
Cooper, M., Martin, R., Lyapustin, A., McLinden, C., 2018. Assessing snow extent data sets over North America to inform trace gas retrievals from solar backscatter. Atmos.

Meas. Tech. 11, 2983–2994.
Croft, H., Chen, J.M., Zhang, Y., Simic, A., 2013. Modelling leaf chlorophyll content in broadleaf and needle leaf canopies from ground, CASI, Landsat TM 5 and MERIS reflectance data. Remote Sens. Environ. 133, 128–140.
Di Bella, C.M., Paruelo, J.M., Becerra, J.E., Bacour, C., Baret, F., 2004. Effect of senescent leaves on NDVI-based estimates of f APAR: experimental and modelling evidences. Int. J. Remote Sens. 25, 5415–5427.
Dong, J., Xiao, X., Wagle, P., Zhang, G., Zhou, Y., Jin, C., Torn, M.S., Meyers, T.P., Suyker, A.E., Wang, J., Yan, H., Biradar, C., III, B.M., 2015. Comparison of four EVI-based models for estimating gross primary production of maize and soybean croplands and tallgrass prairie under severe drought. Remote Sens. Environ. 162, 154–168.
Epstein, H.E., Bhatt, U.S., Raynolds, M.K., Walker, D.A., Bieniek, P.A., Tucker, C.J., Pinzon, J., Myers-Smith, I.H. (Eds.), 2015. Tundra Greenness. NOAA, Silver Spring, MD Available at. http://www.arctic.noaa.gov/reportcard/.
Fang, H., Baret, F., Plummer, S., Schaepman-Strub, G., 2019. An overview of global leaf area index (LAI): methods, products, validation, and applications. Rev. Geophys. 57 (018RG000608).
Fisher, J.B., Melton, F., Middleton, E., Hain, C., Anderson, M., Allen, R., McCabe, M.F., Hook, S., Baldocchi, D., Townsend, P.A., Kilic, A., Tu, K., Miralles, D.D., Perret, J., Lagouarde, J.-P., Waliser, D., Purdy, A.J., French, A., Schimel, D., Famiglietti, J.S., Stephens, G., Wood, E.F., 2017. The future of evapotranspiration: global requirements for ecosystem functioning, carbon and climate feedbacks, agricultural management, and water resources. Water Resour. Res. 53, 2618–2626.
Frouin, R., Pinker, R.T., 1995. Estimating Photosynthetically Active Radiation (PAR) at the earth's surface from satellite observations. Remote Sens. Environ. 51, 98–107.
Gamon, J.A., Huemmrich, K.F., Stone, R.S., Tweedie, C.E., 2013. Spatial and temporal variation in primary productivity (NDVI) of coastal Alaskan tundra: decreased vegetation growth following earlier snowmelt. Remote Sens. Environ. 129, 144–153.
Gao, B.-C., Davis, C.O., 1997. Development of a line-by-line-based atmosphere removal algorithm for airborne and spaceborne imaging spectrometers. SPIE 3118, 132–141.
Gao, B.-C., Heidebrecht, K.H., Goetz, A.F.H., 1993. Derivation of scaled surface reflectances from AVIRIS data. Remote Sens. Environ. 44, 165–178.
Gao, F., Anderson, M.C., Zhang, X., Yang, Z., Alfieri, J.G., Kustas, W.P., Mueller, R., Johnson, D.M., Prueger, J.H., 2017. Toward mapping crop progress at field scales through fusion of Landsat and MODIS imagery. Remote Sens. Environ. 188, 9–25.
Gelman, A., Carlin, J.B., Stern, H.S., Rubin, D.B., 2000. Markov chain simulation. In: Gelman, A., Carlin, J.B., Stern, H.S., Rubin, D.B. (Eds.), Bayesian Data Analysis. Champman & Hall/CRC, New York.
Gobron, N., Pinty, B., Aussedat, O., Taberner, M., Faber, O., Mélin, F., Lavergne, T., Robustelli, M., Snoeij, P., 2008. Uncertainty estimates for the FAPAR operational products derived from MERIS - impact of top-of-atmosphere radiance uncertainties and validation with field data. Remote Sens. Environ. 112, 1871–1883.
Goel, N.S., Deering, D.W., 1985. Evaluation of a canopy reflectance model for LAI estimation through its inversion. IEEE Trans. Geosci. Remote Sens. 23, 674–684.
Goetz, S.J., Bunn, A.G., Fiske, G.J., Houghton, R.A., 2005. Satellite-observed photosynthetic trends across boreal North America associated with climate and fire disturbance. PNAS 102, 13521–13525.
Goswami, S., Gamon, J., Tweedie, C.E., 2011. Surface hydrology of an arctic ecosystem: multi-scale analysis of a flooding and draining experiment using spectral reflectance. J. Geophys. Res. 116, G00I07.
Goward, S.N., Huemmrich, K.F., 1992. Vegetation canopy PAR absorptance and the normalized difference vegetation index - an assessment using the SAIL model. Remote Sens. Environ. 39, 119–140.
Hall, D.K., Riggs, G.A., Salomonson, V.V., 1995. Development of methods for mapping global snow cover using moderate resolution imaging spectroradiometer data. Remote Sens. Environ. 54, 127–140.
Hall, D.K., Riggs, G.A., Salomonson, V.V., DiGirolamo, N.E., Bayr, K.J., 2002. MODIS snow-cover products. Remote Sens. Environ. 83, 181–194.
Hinzman, L.D., Bettez, N.D., Bolton, W.R., Chapin, F.S., Dyurgerov, M.B., Fastie, C.L., Griffith, B., Hollister, R.D., Hope, A., Yoshikawa, K., 2005. Evidence and implications of recent climate change in northern Alaska and other Arctic regions. Climate Change 72, 251–298.
Hobbie, J.E., 1984. The Ecology of Tundra Ponds of the Arctic Coastal Plain: A Community Profile. Fish and Wildlife Service, Washington, DC.
Hollister, Robert D., May, Jeremy L., Kremers, Kelseyann S., Tweedie, Craig E., Oberbauer, Steven F., Liebig, Jennifer A., Botting, Timothy F., Barrett, Robert T., Gregory, Jessica L., 2015. Warming experiments elucidate the drivers of observed directional changes in tundra vegetation. Ecol. Evol. 5 (9), 1881–1895.
Hope, A., Stow, D., 1995. Shortwave reflectance properties of Arctic tundra. In: Reynolds, J., Tenhuenen, J. (Eds.), Landscape Function and Disturbance in Arctic Tundra. Springer, Heidelberg, pp. 155–164.
Hosgood, B., Jacquemoud, S., Andreoli, G., Verdebout, J., Pedrini, G., Schmuck, G., 1995. Leaf Optical Properties EXperiment 93 (LOPEX93). In: European Commision, Joint Research Center, Institute for Remote Sensing Applications, Report EUR 16095 EN.
Huemmrich, K.F., Goward, S.N., 1997. Vegetation canopy PAR absorptance and NDVI: an assessment for ten tree species with the SAIL model. Remote Sens. Environ. 61, 254–269.
Huemmrich, K.F., Gamon, J.A., Tweedie, C.E., Oberbauer, S.F., Kinoshita, G., Houston, S., Kuchy, A., Hollister, R.D., Kwon, H., Mano, M., Harazono, Y., Webber, P.J., Oechel, W.C., 2010. Remote sensing of tundra gross ecosystem productivity and light use efficiency under varying temperature and moisture conditions. Remote Sens. Environ. 114, 481–489.
Huemmrich, K.F., Gamon, J.A., Tweedie, C.E., Campbell, P.K.E., Landis, D.R., Middleton, E.M., 2013. Arctic tundra vegetation functional types based on photosynthetic physiology and optical properties. IEEE Journal of Selected Topics in Applied Earth Observations and Remote Sensing 6, 265–275.
Huete, A., Didan, K., Miura, T., Rodriguez, E.P., Gao, X., Ferreira, L.G., 2002. Overview of the radiometric and biophysical performance of the MODIS vegetation indices. Remote Sens. Environ. 83, 195–213.
Jacquemoud, S., 1993. Inversion of the prospect + sail canopy reflectance model from aviris equivalent spectra - theoretical-study. Remote Sens. Environ. 44, 281–292.
Jacquemoud, S., Baret, F., 1990. PROSPECT - a model of leaf optical-properties spectra. Remote Sens. Environ. 34, 75–91.
Jacquemoud, S., Verhoef, W., Baret, F., Bacour, C., Zarco-Tejada, P.J., Asner, G.P., François, C., Ustin, S.L., 2009. PROSPECT+SAIL models: a review of use for vegetation characterization. Remote Sens. Environ. 113, S56–S66.
Jepsen, S.M., Voss, C.I., Walvoord, M.A., Minsley, B.J., Rover, J., 2013. Linkages between lake shrinkage/expansion and sublacustrine permafrost distribution determined from remote sensing of interior Alaska, USA. Geophys. Res. Lett. 40, 882–887.
Jia, G.J., Epstein, H.E., Walker, D.A., 2003. Greening of arctic Alaska 1981–2001. Geophys. Res. Lett. 30, GL018268.
Jiang, Z., Huete, A.R., Didan, K., Miura, T., 2008. Development of a two-band enhanced vegetation index without a blue band. Remote Sens. Environ. 112, 3833–3845.
Kelly, A.E., Goulden, M.L., 2008. Rapid shifts in plant distribution with recent climate change. Proc. Natl. Acad. Sci. U. S. A. 105, 11823–11826.
Klein, A.G., Hall, D.K., Riggs, G.A., 1998. Improving snow cover mapping in forests through the use of a canopy re¯ectance model. Hydrol. Process. 12, 1723–1744.
Lara, M.J., McGuire, A.D., Euskirchen, E.S., Tweedie, C.E., Hinkel, K.M., 2015. Polygonal tundra geomorphological change in response to warming alters future CO2 and CH4 flux on the Barrow peninsula. Glob. Chang. Biol. 21, 1634–1651.
Lara, M.J., Nitze, I., Grosse, G., Martin, P., McGuire, A.D., 2018. Reduced arctic tundra productivity linked with landform and climate change interactions. Sci. Rep. 8, 1–10.
Lasseur, R., Vannier, C., Lefebvre, J., Longaretti, P.-Y., Lavorel, S., 2018. Landscape- scale modeling of agricultural land use for the quantification of ecosystem services. J. Appl. Remote. Sens. 12, 4602.
Li, X., Xiao, J., He, B., 2018. Chlorophyll fluorescence observed by OCO-2 is strongly related to gross primary productivity estimated from flux towers in temperate forests. Remote Sens. Environ. 204, 659–671.
Liang, S., Li, X., Wang, J., 2012. Advanced Remote Sensing: Terrestrial Information Extraction and Applications. Academic Press, Oxford.
Luus, K.A., Commane, R., Parazoo, N.C., Benmergui, J., Euskirchen, E.S., Frankenberg, C., Joiner, J., Lindaas, J., Miller, C.E., Oechel, W.C., Zona, D., Wofsy, S., Lin, J.C., 2017. Tundra photosynthesis captured by satellite-observed solar-induced chlorophyll fluorescence. Geophys. Res. Lett. 44, 1564–1573.
Lv, Z., Pomeroy, J.W., 2019. Detecting intercepted snow on mountain needleleaf forest canopies using satellite remote sensing. Remote Sens. Environ. 231. https://doi.org/10.1016/j.rse.2019.111222.
Lyapustin, A., Martonchik, J., Wang, Y., Laszlo, I., Korkin, S., 2011a. Multi-Angle Implementation of Atmospheric Correction (MAIAC): part 1. Radiative transfer basis and look-up tables. J. Geophys. Res. 116, D03210.
Lyapustin, A., Wang, Y., Laszlo, I., Kahn, R., Korkin, S., Remer, L., Levy, R., Reid, J.S., 2011b. Multi-Angle Implementation of Atmospheric Correction (MAIAC): part 2. Aerosol algorithm. J. Geophys. Res. 116, D03211.
Lyapustin, A., Wang, Y., Laszlo, I., Hilker, T., Hall, F., Sellers, P., Tucker, J., Korkin, S., 2012. Multi-angle implementation of atmospheric correction for MODIS (MAIAC). 3: atmospheric correction. Remote Sens. Environ. 127, 385–393.
Lyapustin, A., Wang, Y., Korkin, S., Huang, D., 2018. MODIS collection 6 MAIAC algorithm. Atmos. Meas. Tech. 11, 5741–5765.
Major, D.J., Schaalje, G.B., Wiegand, C., Blad, B.L., 1992. Accuracy and sensitivity analyses of SAIL model-predicted reflectance of maize. Remote Sens. Environ. 41, 61–70.
Metropolis, N., Rosenbluth, A.W., Rosenbluth, M.N., Teller, A.H., Teller, E., 1953. Equations of state calculations by fast computing machines. J. Chem. Phys. 21, 1087–1092.
Moulin, S., Kergoat, L., Viovy, N., Dedieu, G., 1997. Global-scale assessment of vegetation phenology using NOAA/AVHRR satellite measurements. J. Clim. 10, 1154–1170.
Myers-Smith, I.H., Kerby, J.T., Phoenix, G.K., Bjerke, J.W., Epstein, H.E., Assmann, J.J., John, C., Andreu-Hayles, L., Angers-Blodin, S., Beck, P.S.A., Berner, L.T., Bhatt, U.S., Bjorkman, A.D., Blok, D., Bryn, A., Christiansen, C.T., Cornelissen, J.H.C., Cunliffe, A.M., Elmendorf, S.C., Forbes, B.C., Goetz, S.J., Hollister, R.D., Jong, R.d., Loranty, M.M., Macias-Fauria, M., Maseyk, K., Normand, S., Olofsson, J., Parker, T.C., Parmentier, F.-J.W., Post, E.S., Schaepman-Strub, G., Stordal, F., Sullivan, P.F., Thomas, H.J.D., Tømmervik, H., Treharne, R., Tweedie, C.E., Walker, D.A., Wilmking, M., Wipf, S., 2019. Complexity Revealed in the Greening of the Arctic. EcoEvoRxiv Preprints. https://ecoevorxiv.org/mzyjk/pp. 1–40.
Myneni, R.B., Keeling, C.D., Tucker, C.J., Asrar, G., Nemani, R.R., 1997. Increased plant growth in the northern high latitudes from 1981 to 1991. Nature 386, 698–702.
Myneni, R.B., Hoffman, S., Knyazikhin, Y., Privette, J.L., Glassy, J., Tian, Y., Wang, Y., Song, X., Zhang, Y., Smith, G.R., Lotsch, A., Friedl, M., Morisette, J.T., Votava, P., Nemani, R.R., Running, S.W., 2002. Global products of vegetation leaf area and fraction absorbed PAR from year one of MODIS data. Remote Sens. Environ. 83, 214–231.
Newnham, G.J., Burt, T., 2001. Validation of a leaf reflectance and transmittance model for three agricultural crop species. International Geoscience and Remote Sensing Symposium 7, 2976–2978.
Nitze, I., Grosse, G., Jones, B., Arp, C., Ulrich, M., Fedorov, A., Veremeeva, A., 2017. Landsat-based trend analysis of lake dynamics across northern permafrost regions. Remote Sens. 9.
Pinker, R.T., Laszlo, I., 1992. Global distribution of photosynthetically active radiation as observed from satellites. J. Clim. 5, 56–65.
Pinker, R.T., Zhao, M., Wang, H., Wood, E.F., 2010. Impact of satellite based PAR on estimates of terrestrial net primary productivity. Int. J. Remote Sens. 31, 5221–5237.
Safari, A., Sohrabi, H., Powell, S., 2018. Comparison of satellite-based estimates of

aboveground biomass in coppice oak forests using parametric, semiparametric, and nonparametric modeling methods. J. Appl. Remote. Sens. 12, 046026.
Salminen, M., Pulliainen, J., Metsämäki, S., Kontu, A., Suokanerva, H., 2009. The behaviour of snow and snow-free surface reflectance in boreal forests: implications to the performance of snow covered area monitoring. Remote Sens. Environ. 113, 907–918.
Salomonson, V., Appel, I., 2004. Estimating fractional snow cover from MODIS using the normalized difference snow index. Remote Sens. Environ. 89, 351–360.
Sims, D.A., Rahman, A.F., Cordova, V.D., El-Masri, B.Z., Baldocchi, D.D., Bolstad, P.V., Flanagan, L.B., Goldstein, A.H., Hollinger, D.Y., Misson, L., Monson, R.K., Oechel, W.C., Schmid, H.P., Wofsy, S.C., Xu, L., 2008. A new model of gross primary productivity for north American ecosystems based solely on the enhanced vegetation index and land surface temperature from MODIS. Remote Sens. Environ. 112, 1633–1646.
Stone, R.S., Dutton, E.G., Harris, J.M., Longenecker, D., 2002. Earlier spring snowmelt in northern Alaska as an indicator of climate change. J. Geophys. Res. 107, 4089.
Stow, D.A., Hope, A., McGuire, D., Verbyla, D., Gamon, J., Huemmrich, F., Houston, S., Racine, C., Sturm, M., Tape, K., Hinzman, L., 2004. Remote sensing of vegetation and land-cover change in Arctic tundra ecosystems. Remote Sens. Environ. 89, 281–308.
Sun, L., Neville, R., Staenz, K., White, H.P., 2008. Automatic destriping of Hyperion imagery based on spectral moment matching. Can. J. Remote. Sens. 34, S68–S81.
Tagliabue, G., Panigada, C., Dechant, B., Baret, F., Cogliati, S., Colombo, R., Migliavacca, M., Rademske, P., Schickling, A., Schüttemeyer, D., Verrelst, J., Rascher, U., Ryu, Y., Rossini, M., 2019. Exploring the spatial relationship between airborne-derived red and far-red sun-induced fluorescence and process-based GPP estimates in a forest ecosystem. Remote Sens. Environ. 231. https://doi.org/10.1016/j.rse.2019.111272.
Tang, X., Bullock, E.L., Olofsson, P., Estel, S., Woodcock, C.E., 2019. Near real-time monitoring of tropical forest disturbance: new algorithms and assessment framework. Remote Sens. Environ. 224, 202–218.
Tao, X., Liang, S., Wang, D., 2015. Assessment of five global satellite products of fraction of absorbed photosynthetically active radiation: intercomparison and direct validation against ground-based data. Remote Sens. Environ. 163, 270–285.
van der Tol, C., Verhoef, W., Rosema, A., 2009a. A model for chlorophyll fluorescence and photosynthesis at leaf scale. Agric. For. Meteorol. 149, 96–105.
van der Tol, C., Verhoef, W., Timmermans, J., Verhoef, A., Su, Z., 2009b. An integrated model of soil-canopy spectral radiances, photosynthesis, fluorescence, temperature and energy balance. Biogeosciences 6, 3109–3129.
van der Tol, C., Berry, J.A., Campbell, P.K.E., Rascher, U., 2014. Models of fluorescence and photosynthesis for interpreting measurements of solar-induced chlorophyll fluorescence. J. Geophys. Res. Biogeosci. 119, 2312–2327.
Tucker, C.J., 1979. Red and photographic infrared linear combinations for monitoring vegetation. Remote Sens. Environ. 8, 127–150.
Verhoef, W., 1984. Light-scattering by leaf layers with application to canopy reflectance modeling - the SAIL model. Remote Sens. Environ. 16, 125–141.
Verhoef, W., 1985. Earth observation modeling based on layer scattering matrices. Remote Sens. Environ. 17, 165–178.
Vermote, E.F., Tanre, D., Deuze, J.L., Herman, M., Morcrette, J.J., 1997. Second simulation of the satellite signal in the solar spectrum, 6S: an overview. IEEE Trans. Geosci. Remote Sens. 35, 675–686.
Walther, S., Voigt, M., Thum, T., Gonsamo, A., Zhang, Y., Köhler, P., Jung, M., Varlagin, A., Guanter, L., 2016. Satellite chlorophyll fluorescence measurements reveal large-scale decoupling of photosynthesis and greenness dynamics in boreal evergreen forests. Glob. Chang. Biol. 22, 2979–2996.
Wang, Y., 2002. Assesment of the MODIS LAI and FPAR algorithm: Retrieval quality, theoretical basis and validation. In: Geography. Boston University, Boston, pp. 1–152.
Waring, R., Landsberg, J., Linder, S., 2016. Tamm review: insights gained from light use and leaf growth efficiency indices. For. Ecol. Manag. 379, 232–242.
Webber, P.J., Miller, P.C., Chapin III, F.S., McCown, B.H., 1980. The vegetation: pattern and succession. In: Alaska, J.B., Miller, P.C., Tieszen, L.L., Bunnell, F.L. (Eds.), An Arctic Ecosystem, the Coastal Tundra at Barrow. Dowden, Hutchison, and Ross, Inc, Stroudsberg, PA, USA, pp. 186–218.
Xiao, X.M., Hollinger, D., Aber, J., Goltz, M., Davidson, E.A., Zhang, Q., Moore, B., 2004a. Satellite-based modeling of gross primary production in an evergreen needleleaf forest. Remote Sens. Environ. 89, 519–534.
Xiao, X.M., Zhang, Q.Y., Braswell, B., Urbanski, S., Boles, S., Wofsy, S., Moore, B., Ojima, D., 2004b. Modeling gross primary production of temperate deciduous broadleaf forest using satellite images and climate data. Remote Sens. Environ. 91, 256–270.
Xiao, Z., Liang, S., Sun, R., Wang, J., Jiang, B., 2015. Estimating the fraction of absorbed photosynthetically active radiation from the MODIS data based GLASS leaf area index product. Remote Sens. Environ. 171, 105–117.
Yang, Y., Anderson, M., Gao, F., Hain, C., Kustas, W., Meyers, T., Crow, W., Finocchiaro, R., Otkin, J., Sun, L., Yang, Y., 2017. Impact of tile drainage on evapotranspiration in South Dakota, USA, based on high spatiotemporal resolution evapotranspiration time series from a multisatellite data fusion system. IEEE Journal of Selected Topics in Applied Earth Observation Remote Sensing (JSTARS) 10, 2550–2564.
Yang, K., Ryu, Y., Dechant, B., Berry, J.A., Hwang, Y., Jiang, C., Kang, M., Kim, J., Kimm, H., Kornfeld, A., Yang, X., 2018. Sun-induced chlorophyll fluorescence is more strongly related to absorbed light than to photosynthesis at half-hourly resolution in a rice paddy. Remote Sens. Environ. 216, 658–673.
Zhan, X., Sohlberg, R.A., Townshend, J.R.G., DiMiceli, C., Carroll, M.L., Eastman, J.C., Hansen, M.C., DeFries, R.S., 2002. Detection of land cover changes using MODIS 250 m data. Remote Sens. Environ. 83, 336–350.
Zhang, X., Friedl, M.A., Schaaf, C.B., Strahler, A.H., Hodges, J.C.F., Gao, F., Reed, B.C., Huete, A., 2003. Monitoring vegetation phenology using MODIS. Remote Sens. Environ. 84, 471–475.
Zhang, Q., Xiao, X.M., Braswell, B., Linder, E., Baret, F., Moore, B., 2005. Estimating light absorption by chlorophyll, leaf and canopy in a deciduous broadleaf forest using MODIS data and a radiative transfer model. Remote Sens. Environ. 99, 357–371.
Zhang, Q., Xiao, X., Braswell, B., Linder, E., Ollinger, S., Smith, M.L., Jenkins, J.P., Baret, F., Richardson, A.D., Moore, B., Minocha, R., 2006. Characterization of seasonal variation of forest canopy in a temperate deciduous broadleaf forest, using daily MODIS data. Remote Sens. Environ. 105, 189–203.
Zhang, Q., Middleton, E.M., Margolis, H.A., Drolet, G.G., Barr, A.A., Black, T.A., 2009. Can a MODIS-derived estimate of the fraction of PAR absorbed by chlorophyll ($FAPAR_{chl}$) improve predictions of light-use efficiency and ecosystem photosynthesis for a boreal aspen forest? Remote Sens. Environ. 113, 880–888.
Zhang, Q., Middleton, E.M., Gao, B.-C., Cheng, Y.-B., 2012. Using EO-1 hyperion to simulate HyspIRI products for a coniferous forest: the fraction of PAR absorbed by chlorophyll ($fAPAR_{chl}$) and leaf water content (LWC). IEEE Trans. Geosci. Remote Sens. 50, 1844–1852.
Zhang, Q., Middleton, E.M., Cheng, Y.-B., Landis, D.R., 2013. Variations of foliage chlorophyll fAPAR and foliage non-chlorophyll fAPAR ($fAPAR_{chl}$, $fAPAR_{non\text{-}chl}$) at the Harvard Forest. IEEE Journal of Selected Topics in Applied Earth Observations and Remote Sensing 6, 2254–2264.
Zhang, Q., Cheng, Y.-B., Lyapustin, A.I., Wang, Y., Gao, F., Suyker, A., Verma, S., Middleton, E.M., 2014a. Estimation of crop gross primary production (GPP): fAPARchl versus MOD15A2 FPAR. Remote Sens. Environ. 153, 1–6.
Zhang, Q., Cheng, Y.-B., Lyapustin, A.I., Wang, Y., Xiao, X., Suyker, A., Verma, S., Tan, B., Middleton, E.M., 2014b. Estimation of crop gross primary production (GPP): I. Impact of MODIS observation footprint area and impact of vegetation BRDF characteristics. Agric. For. Meteorol. 191, 51–63.
Zhang, Q., Cheng, Y.-B., Lyapustin, A., Wang, Y., Zhang, X., Suyker, A., Verma, S., Shuai, Y., Middleton, E., 2015. Estimation of crop gross primary production (GPP): II. Do the scaled vegetation indices improve performance? Agric. For. Meteorol. 200, 1–8.
Zhang, Q., Middleton, E.M., Cheng, Y.-B., Huemmrich, K.F., Cook, B.D., Corp, L.A., Kustas, W.P., Russ, A.L., Prueger, J.H., Yao, T., 2016. Integrating chlorophyll fAPAR and nadir photochemical reflectance index from EO-1/Hyperion to predict cornfield daily gross primary production. Remote Sens. Environ. 186, 311–321.
Zhang, L., Feng, H., Dong, Q., Jin, N., Zhang, T., 2018a. Mapping irrigated and rainfed wheat areas using high spatial–temporal resolution data generated by Moderate Resolution Imaging Spectroradiometer and Landsat. J. Appl. Remote. Sens. 12, 04602.
Zhang, Y., Xiao, X., Wolf, S., Wu, J., Wu, X., Gioli, B., Wohlfahrt, G., Cescatti, A., Tol, C., Zhou, S., Gough, C.M., Gentine, P., Zhang, Y., Steinbrecher, R., Ardö, J., 2018b. Spatio-temporal convergence of maximum daily light-use efficiency based on radiation absorption by canopy chlorophyll. Geophys. Res. Lett. 45, 3508–3519.
Zhao, M., Running, S., 2010. Drought-induced reduction in global terrestrial net primary production from 2000 through 2009. Science 329, 940–943.
Zhou, L., Tucker, C.J., Kaufmann, R.K., Slayback, D., Shabanov, N.V., Myneni, R.B., 2001. Variations in northern vegetation activity inferred from satellite data of vegetation index during 1981 to 1999. J. Geophys. Res. 106, 20069–20083.
Zhou, H., Aizen, E., Aizen, V., 2013. Deriving long term snow cover extent dataset from AVHRR and MODIS data: Central Asia case study. Remote Sens. Environ. 136, 146–162.